Master Laboratory

Optical Pumping

Group 18

Performed on April 5th–April 9th
under supervision of

Abstract

Optical pumping is a method of changing occupation numbers of atomic system by irradiation of the system with characteristic light. In the experiment this report documents the method was used for determining several characteristics of Rubidium (^{85}Rb and ^{87}Rb) as well as measuring earth's magnetic field strength in various directions.

The hyperfine structure of ^{85}Rb and ^{87}Rb was investigated and six out of eigth expected spectral lines could be resolved. With the frequency of the hyperfine structure energy shifts we were able to calculate three out of four hyperfine structure constants $A_{^{87}\mathrm{Rb},^2\mathrm{S}_{1/2}} = (1.44 \pm 0.03) \times 10^{-5}\,\mathrm{eV}$, $A_{^{87}\mathrm{Rb},^2\mathrm{P}_{1/2}} = (1.54 \pm 0.27) \times 10^{-6}\,\mathrm{eV}$, and $A_{^{85}\mathrm{Rb},^2\mathrm{S}_{1/2}} = (4.71 \pm 0.15) \times 10^{-6}\,\mathrm{eV}$, the first two being in a 2-σ-environment and the third in a 4-σ-environment of the literature value.

With optical pumping under double resonance with we determined the nuclear spins of ^{85}Rb and ^{87}Rb to be $I_{^{85}\mathrm{Rb}} = 2.51 \pm 0.03$ and $I_{^{87}\mathrm{Rb}} = 1.49 \pm 0.03$, respectively; the values are extremely well compatible with the literature values and feature a relative error of $\approx 2\,\%$. Further, earths magnetic field was measured with optical pumping under double resonance to be $B_{\mathrm{vert}} = (33.9 \pm 0.5)\,\mu\mathrm{T}$, $B_{\mathrm{hor}} = (5.6 \pm 1.1)\,\mu\mathrm{T}$ which deviates by about 18 standard deviations from the literature value.

Leveraging the precession of the ensembles spin in the vertical component of earth's magnetic field, the absolute value of the latter was determined to be $B_{\mathrm{vert}} = (32.6 \pm 1.4)\,\mu\mathrm{T}$, deviating 7-$\sigma$ from the literature value but compatible with the value from the double resonance part of the experiment.

With the methods of Dehmelt and Franzen, the relaxation time of the system was determined to be $T_{\mathrm{R}}^{^{85}\mathrm{Rb}} = (4.3 \pm 2.5)\,\mathrm{ms}$, $T_{\mathrm{R}}^{^{87}\mathrm{Rb}} = (-5.1 \pm 2.4)\,\mathrm{ms}$, and $T_{\mathrm{R}} = (8.5 \pm 2.5)\,\mathrm{ms}$, deviating at most 5-$\sigma$ from the literature value. While the methods could be succesfully replicated, the results are not consistent with each other.

Contents

1. Introduction

Light especially in form of laser light is an excellent tool to manipulate matter on atomic scale. One method to use light to manipulate atoms is called optical pumping and is the focus of this report. During optical pumping the population some of the energetic levels of atoms get overpopulated while others get pumped emptied by emitting resonant light at the atoms. The idea of optical pumping was developed by Prof. Kastler in the year 1949 and in the following years Brossel, Kastler and Winter, as well as Hawkins and Dicke were able to polarise the ground state of atoms by optical pumping in experiments.

Since then, the principal of optical pumping could be used to measure a variety of atomic quantities of several isotopes, as for example the nuclear spin and hyperfine structure intervals which will also be done in this report.

In this report a experiment is presented and analyzed which uses the principle of optical pumping to measure the nuclear spin and hyperfine structure constants of the isotopes ^{85}Rb and ^{87}Rb. Further, the magnetic stray fields present at the experiment will be measured and compared to the magnetic field of the earth in Freiburg. At last, the relaxation time of the pumped ensemble will be measured once with Dehmelt's method using the inversion of a induced magnetic field and once with Franzen's method measuring the relaxation by turning the pumping light on and off.

The report itself is structured as follows: In section 2 the necessary theoretical background to understand the measurements done in this experiment and its results will be provided. Afterwards, the setup of the experiment and the procedure how the experiment was carried out will be explained in section 3. This is followed by the presentation of the analysis of the data measured in section 4. At the end in section 5 we will summarize the results obtained by the experiment and discuss their quality and the experiment over all.

2. Theory

In the following sections, some information specific to the optical pumping experiment is summarized. The summary is closely based on the Staatsexamen [1] which should be taken as basic reference for the following paragraphs if not otherwise indicated.

2.1. Hyperfine structure

The electric charge of the nucleus of an atom generates a Coulomb potential. When considering the orbiting electrons classically, there are only discrete "allowed" orbits. The difference in the energy levels of those orbits can be seen as spectral lines. Due to the magnetic interaction of spin angular momentum and orbital angular momentum, the energy levels of the atom system are degenerate. This so called fine structure can be measured by increasing the frequency resolution as the energy shift of this effect is small in comparison with the energy difference of the original energy levels. By further increasing the spectral resolution another structure becomes visible: the hyperfine structure. The hyperfine structure is caused by the interaction of the nuclear spin I with the total angular momentum J of the electron's hull.

Total electronic angular momentum The total angular momentum $\boldsymbol{j}$ of a single electron is defined as the sum of its spin angular momentum $\boldsymbol{s}$ and its orbital angular momentum $\boldsymbol{l}$:

$$\boldsymbol{j} = \boldsymbol{l} + \boldsymbol{s}. \tag{1}$$

If the quantum system consists of multiple electrons, their spin angular momenta may be summed to yield a total spin angular momentum $\boldsymbol{S}$; similarly, by summing all the electron's orbital angular momenta, one obtains the total orbital angular momentum $\boldsymbol{L}$. As the total orbital angular momentum and the total spin angular momentum couple together in L-S-coupling to a total angular momentum $\boldsymbol{J} = \boldsymbol{L} + \boldsymbol{S}$, the total magnetic moment of the multi-electron system is given by

$$\boldsymbol{\mu}_J = -\frac{\mu_\mathrm{B}}{\hbar} g_J \boldsymbol{J}, \tag{2}$$

$\mu_\mathrm{B} = e\hbar/2m_\mathrm{e}$ is known as Bohr magneton, while g_J is the Landé g-factor which can be calculated from the quantum numbers J, L, and S:

$$g_J = 1 + \frac{J(J+1) + S(S+1) - L(L+1)}{2J(J+1)}. \tag{3}$$

Angular momentum of the nucleus Protons and neutrons in the atomic nucleus are both spin-$\frac{1}{2}$-particles and feature an orbital angular momentum. The resulting angular momentum $\boldsymbol{I}$ with

$$|\boldsymbol{I}| = \sqrt{I(I+1)}\hbar \tag{4}$$

takes on only half-integer values between 0 and $\frac{15}{2}$. As $\boldsymbol{I}$ is an orbital angular momentum operator, its z-component only measures discrete values $\hbar m_I$, where m_I ist the magnetic

quantum number of $\boldsymbol{I}$ and takes on values between $-I$ and I in integer steps. Due to the nucleus' charge, the nucleus induces a magnetic moment

$$\boldsymbol{\mu}_I = \gamma \boldsymbol{I} = -\frac{\mu_\mathrm{K}}{\hbar} g_i \boldsymbol{I}. \tag{5}$$

The constant $\gamma = -g_I \mu_\mathrm{K}/\hbar$ is known as the gyromagnetic ratio. Meanwhile, g_I is known as the nuclear g-factor and it is characteristic for each nucleus, meaning that it can't be calculated from other quantum numbers. Analogously to the Bohr magneton, $\mu_\mathrm{K} = e\hbar/(2m_\mathrm{p})$ refers to the nuclear magneton and is calculated using the mass m_p of the proton. The z-component of the magnetic moment of the nucleus can be calculated from the formulas already given:

$$(\mu_I)_z = \gamma I_z = \gamma \hbar m_I = g_I \mu_\mathrm{K} m_I. \tag{6}$$

The magnitude of the nucleus' magnetic moment is usually 3 orders lower than its electronic counterpart.

Hyperfine interaction The hyperfine structure already mentioned at the beginning of the section originates from the interaction of the nuclear magnetic moment with the electromagnetic field of the electronic hall. Due to the magnitude of the nuclear magnetic moment being reduced by 3 orders of magnitude, the effect is very hard to detect. The total angular momentum of the electrons $\boldsymbol{J}$ couples with the total nuclear spin $\boldsymbol{I}$ to a new total angular momentum of the atom as a whole $\boldsymbol{F}$:

$$\boldsymbol{F} = \boldsymbol{I} + \boldsymbol{J}. \tag{7}$$

For quantum number F of $\boldsymbol{F}$ it holds that

$$|I - J| \leq F \leq I + J \tag{8}$$

as $\boldsymbol{F}$ is the sum of angular momenta. This means that F can take on exactly $2 \cdot \min\{I, J\} + 1$ possible values. When the magnetic field $\boldsymbol{B}_J$ of the electronic hull is present, the energy due to the interaction of the atom's magnetic moment is given by

$$E_\mathrm{HFS} = -\boldsymbol{I} \cdot \boldsymbol{B}_J. \tag{9}$$

Expressed in the quantum numbers and using eqs. (4) and (5), we arrive at

$$E_\mathrm{HFS} = -|\boldsymbol{\mu}_I||\boldsymbol{B}_J| \cos(\angle(\boldsymbol{I}, \boldsymbol{J})) \tag{10}$$

$$= g_I \mu_\mathrm{K} \sqrt{I(I+1)} |\boldsymbol{B}_J| \cos(\angle(\boldsymbol{I}, \boldsymbol{J})). \tag{11}$$

By taking the squared absolute of eq. (7) and imposing $|\boldsymbol{F}| = \hbar\sqrt{F(F+1)}$, one obtains

$$\cos(\angle(\boldsymbol{I}, \boldsymbol{J})) = \frac{I(I+1) + J(J+1) - F(F+1)}{2\sqrt{I(I+1) + J(J+1)}}. \tag{12}$$

Inserting this relation into the interaction energy between the magnetic field of the electrons and the nuclear spin $\boldsymbol{I}$, this gives

$$E_{\mathrm{HFS}} = \frac{A}{2}\left[F(F+1) - I(I+1) - J(J+1)\right], \tag{13}$$

where A is known as interval or hyperfine constant:

$$A = \frac{\mu_{\mathrm{K}} g_I B_J}{\sqrt{J(J+1)}}. \tag{14}$$

Using this hyperfine constant, the energy difference between two neighbouring atomic states, say, the state with quantum number F and the one with $F+1$, is given by

$$E_{\mathrm{HFS}}(F+1) - E_{\mathrm{HFS}}(F) = A(F+1). \tag{15}$$

Zeeman effect of the hyperfine structure The degeneracy of the $2F+1$ hyperfine-structure terms can be lifted by applying an external magnetic field: The $2F+1$ energy levels are split according to the magnetic quantum number m_F. This so-called Zeeman effect only occurs, if the energy of the atom in the external magnetic field is small in comparison to the coupling of $\boldsymbol{I}$ and $\boldsymbol{J}$. This condition may be written as $g_J \mu_{\mathrm{B}} B \ll A$, where A is the hyperfine constant. The total angular momentum $\boldsymbol{F}$ is quantized relative to the z-component (here: the direction of the external magnetic field) such that F_z may take on $2F+1$ different values. By averaging the interaction $E_B = -\boldsymbol{\mu}_F \cdot \boldsymbol{B}$ over time, where $\boldsymbol{\mu}_F = \boldsymbol{\mu}_I + \boldsymbol{\mu}_J$, and using perturbation theory in B, one obtains

$$E_B = g_F \mu_{\mathrm{B}} B m_F, \tag{16}$$

where g_F is the atom's total Landé factor:

$$\begin{aligned} g_F = g_J \frac{F(F+1) + J(J+1) - I(I+1)}{2F(F+1)} \\ - g_I \frac{\mu_{\mathrm{K}}}{\mu_{\mathrm{B}}} \frac{F(F+1) + I(I+1) - J(J+1)}{2F(F+1)}. \end{aligned} \tag{17}$$

As the ratio $\frac{\mu_{\mathrm{K}}}{\mu_{\mathrm{B}}} \approx \frac{1}{2000}$ is negligible, the second term can be neglected as well. In our experiment our focus is on Rubidium, which has an electronic total angular momentum of $J = \frac{1}{2}$. Then, by considering the cases $F = I + \frac{1}{2}$ and $F = I - \frac{1}{2}$ seperately and neglecting the second summand, eq. (17) may be simplified to

$$g_F = \pm \frac{g_J}{2(I + \frac{1}{2})}. \tag{18}$$

This allows us to explicitly calculate the energy difference between two neighbouring Zeeman states (with $\Delta m_F = 1$) by inserting this relation into eq. (16):

$$\Delta\nu h = \Delta E_B = E_B(m_F + 1) - E_B(m_F) = \frac{g_J}{2(I + \frac{1}{2})} \mu_{\mathrm{B}} B. \tag{19}$$

Table 1 shows an overview over the quantum numbers that are relevant for our experiment while fig. 1 shows the relevant term schema. The spectral lines of the hyperfine structure transitions can be seen in fig. 2 for both Rubidium isotopes.

Table 1: Overview over the quantum numbers of the Isotopes of Rubidium that we consider for our experiment.

Isotope	I	Term	S	L	J	g_J	F	g_F
^{85}Rb	$\frac{5}{2}$	$^2S_{1/2}$	$\frac{1}{2}$	0	$\frac{1}{2}$	2	2	$-\frac{1}{3}$
							2	$\frac{1}{3}$
		$^2P_{1/2}$	$\frac{1}{2}$	1	$\frac{1}{2}$	$\frac{2}{3}$	2	$-\frac{1}{9}$
							3	$\frac{1}{9}$
^{87}Rb	$\frac{3}{2}$	$^2S_{1/2}$	$\frac{1}{2}$	0	$\frac{1}{2}$	2	1	$-\frac{1}{2}$
							2	$\frac{1}{2}$
		$^2P_{1/2}$	$\frac{1}{2}$	1	$\frac{1}{2}$	$\frac{2}{3}$	1	$-\frac{1}{6}$
							2	$\frac{1}{6}$

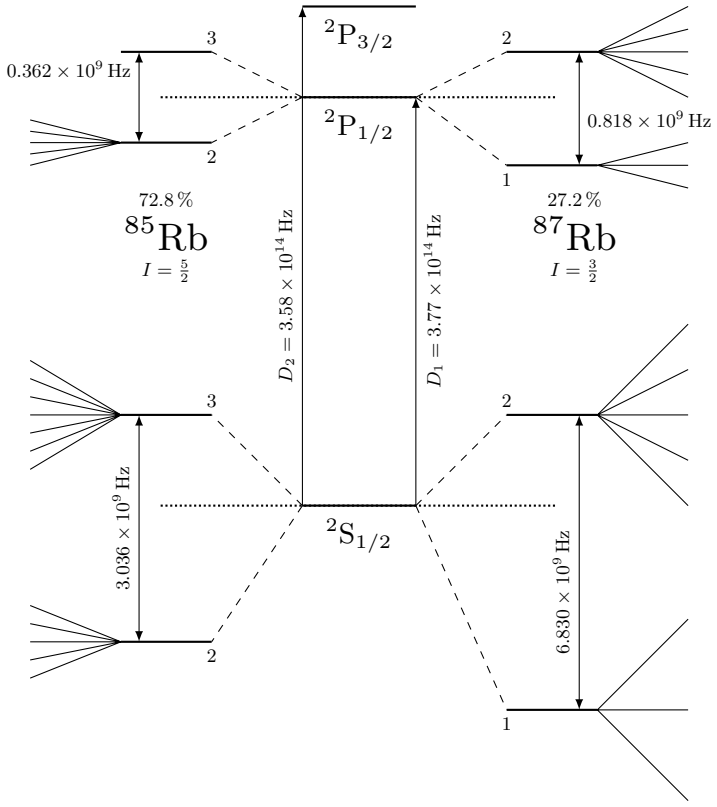

Figure 1: Term schema of both Rubidium isotopes. The energy shifts are not up to scale. Adapted from the Staatsexamen [1].

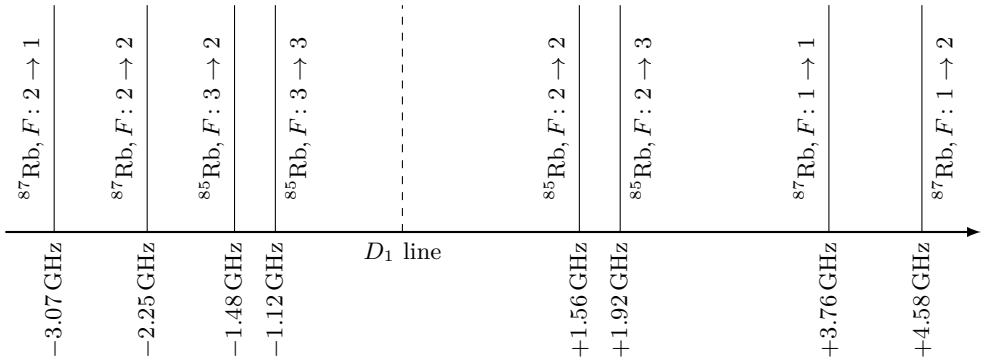

Figure 2: Transition frequencies of the hyperfine transition between the $^2S_{1/2}$ and the $^2P_{1/2}$ terms for both Rubidium isotopes.

2.2. Optical pumping

Optical pumping refers to the principle that the statistical occupation of energy levels of a system of atoms is changed by irradiation with light of specific characteristics. While some energy levels get occupied more, others are emptied over time.

Optical pumping in a simplified model The principle of optical pumping will be explained using a simplified model: We assume that the nucleus of the Rubidium atoms do not posess a magnetic moment. This results in the abscence of a coupling between the nuclear magnetic moment and the electron's field, i. e. the hyperfine structure is missing. The Zeeman energy levels will instead be split by an external magnetic field. The splitting is visualized on the left in fig. 3. The figure also shows the four possible transitions. With linearly polarized light (denoted here by π), the magnetic quantum number m_J does not change in the transition. The magnetic quantum number increases ($\Delta m_J = 1$) for circularly polarized light in the right hand sense and decreases ($\Delta m_J = -1$) for circularly polarized light in the left hand sense. The principle of optical pumping can be understood by considering the graphic on the left in fig. 3. If one irradiates the system only using π-light, the energy states will not be occupied by a distribution different from the statistical one due to symmetry. By exposing the system to σ^+-light, however, changes the distribution: This is because the only state which can absorb σ^+-light is the $^2S_{1/2}, m_J = -\frac{1}{2}$ state which transitions to the $^2P_{1/2}, m_J = +\frac{1}{2}$. The excited state will then decay to the $^2S_{1/2}, m_J = -\frac{1}{2}$ state with a probability of 66 % or to the $^2S_{1/2}, m_J = +\frac{1}{2}$ state with a probability of 33 %. The latter state, however, will not get excited to the $^2P_{1/2}$ state by the σ^+-light. Further, due to the selection rules, the state cannot transition to the other $^2S_{1/2}$-state. Thus, the state most encountered after continuos irradiation of the system with σ^+-light will be the $^2S_{1/2}, m_J = +\frac{1}{2}$ state while the other $^2S_{1/2}, m_J = +\frac{1}{2}$ state will be almost empty in theory. In praxis, however, there exist so-called relaxation processes which inhibit the pumping process to some extent and are described later in this section. Nevertheless, the optical pumping causes most

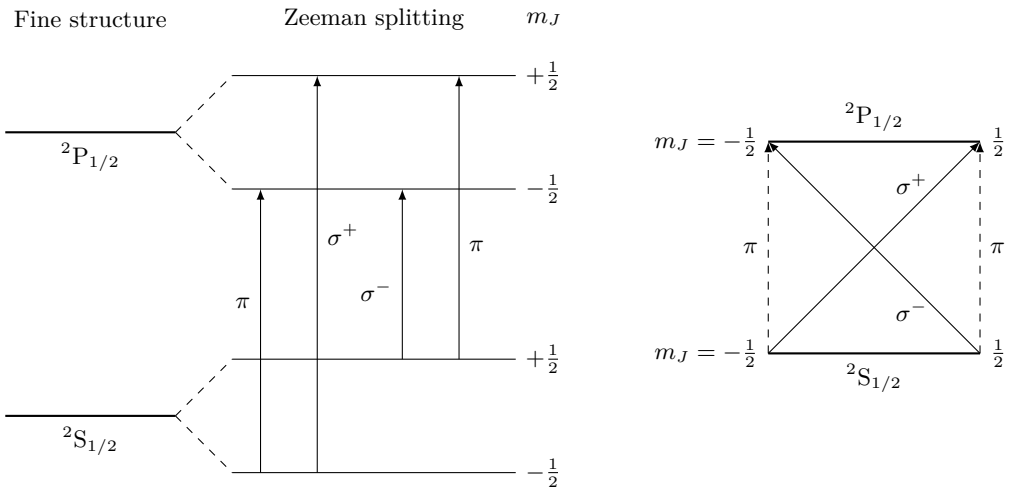

Figure 3: Simplified terms of Rubidium without hyperfine structure (left: vertically ordered by energy, right: rearranged by magnetic quantum number). Adapted from the Staatsexamen [1].

of the atoms' spins in the system to be oriented in the same direction.

Zeeman pumping with Rubidium Now we consider the process of optical pumping of Rubidium where we do not neglect the nuclear spin. To be more specific, we focus on ^{87}Rb in the following. As the hyperfine structure's energy levels are split in an external magnetic field, there are more transitions to consider than in the simplified case. Still, fig. 4 shows some of the possible transitions of ^{87}Rb when irradiated with σ^+-light. Under exposure to this light, atoms in the $^2S_{1/2}$ state transition into a Zeeman niveau in the $^2P_{1/2}$ state while the magnetic quantum number m_F must increase by one. Thus, a transition from the $^2S_{1/2}, F = 2, m_F = +2$ state is not possible through σ^+-light. An excited state may decay into a lower state under the selection rule $\Delta m_F = -1, 0, +1$. This means that the probability to decay into a state with $m_F > 1$ is 2/3. Thus, atoms tend to accumulate in the $^2S_{1/2}, F = 2, m_F = +2$ state where they can't escape due to the selection rules and the nature of the irradiating light, exactly like in the case where the nuclear spin was neglected.

Analogously, when considering ^{85}Rb, the state that is occupied the most is the state with $^2S_{1/2}, F = 3, m_F = +3$.

2.3. Relaxation processes

As already mentioned in the preceding paragraphs, relaxation processes act contrary to the pumping process: while the pumping process results in one state occupied more that other states, relaxation processes strive towards a statistical equilibrium. In the following, a selection of several of such processes is briefly presented.

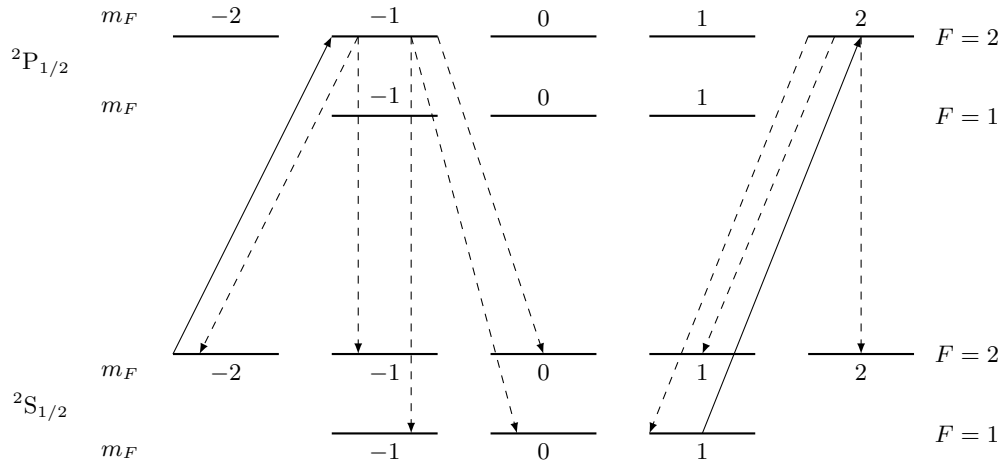

Figure 4: Polarisation schema of ^{87}Rb under irradiation with σ^+-light. Dashed lines signify decays in lower states while lines that are drawn through refer to transitions caused by σ^+-light.

- Collision with the wall: The Rubidium of our experiment is enclosed in a glass sphere which also contains some buffer gases (here, they are given by noble gases). If a Rubidium atom collides with the glass wall, its orientation is presumably lost. If one assumes the pressure inside the glass sphere to be sufficiently high, the collisions with the glass wall can be modeled via diffusion: If n is the difference in the occupation numbers of the oriented and un-oriented states, we have

$$\frac{\partial n}{\partial t} = D\nabla^2 n, \tag{20}$$

  where D is diffusion constant which depends on the pressure inside the glass sphere.

- Collision with buffer gas atoms: Although noble gases don't feature a magnetic field, the orientation of the Rubidium atoms can still be influenced by direct collisions of Rubidium atoms with buffer gas atoms. However, a re-orientation of the Rubidium spin is relatively rare due to the fact that both the wave function of the ground state of Alkali atoms and noble gases is spherically symmetric. The relaxation process can then happen only due to weak dipole-dipole interactions or spin-orbit interaction.

- Spin interchange: If two Rubidium atoms collide, their valence electrons may interchange their spin. Even though the electron spin of the total ensemble remains unchanged, the total nuclear and the electronic angular momentum is uncoupled which results in the occupation numbers of the $F = I \pm \frac{1}{2}$ states to compensate. This is also known as ΔF-pumping.

Relaxation times In order to better quantify the evolution of the occupation of our states in time, we will take a more general point of view and consider a system with

a state from which pumping is possible and another state that we can pump in. We call the occupation numbers of these states N_- and N_+, respectively. Further, we call $n = N_+ - N_-$ the difference in the occupation numbers and $N = N_+ + N_-$ the total occupation number which we assume to be constant. Then, the pumping process obeys the following differential equation:

$$\left(\frac{\mathrm{d}n}{\mathrm{d}t}\right)_{\text{pumping}} = \frac{N-n}{T_\mathrm{P}}. \tag{21}$$

T_P is the so-called pumping time which is proportional to the inverse of the intensity I of the pumping light:

$$T_\mathrm{P} = \frac{1}{\alpha I}, \tag{22}$$

where α is a proportionality constant. Now we take relaxation processes into account. It is reasonable to assume that the rate of change in the difference in the occupation number is proportional to the value of that number as we are dealing with the process of striving toward a statistical equilibrium. Thus,

$$\left(\frac{\mathrm{d}n}{\mathrm{d}t}\right)_{\text{relax}} = -\frac{n}{T_\mathrm{R}}. \tag{23}$$

T_R is the so-called relaxation time. The pure relaxation differential equation can be easily solved by

$$n(t) = n_0 \exp\!\left(-\frac{t}{T_\mathrm{R}}\right). \tag{24}$$

As both pumping and relaxation processes are continuously happening at the same time, we consider the sum of the differential equations in eqs. (21) and (23):

$$\left(\frac{\mathrm{d}n}{\mathrm{d}t}\right)_{\text{orientation}} = \frac{N-n}{T_\mathrm{P}} - \frac{n}{T_\mathrm{R}}. \tag{25}$$

In the case of a dynamical equilibrium, the difference in the occupation numbers doesn't change anymore and is at a maximum n_max. Solving $\frac{\mathrm{d}n}{\mathrm{d}t} = 0$ gives

$$n_\mathrm{max} = \frac{N}{1 + \frac{T_\mathrm{P}}{T_\mathrm{R}}}. \tag{26}$$

Introducing a time constant τ by the relation

$$\frac{1}{\tau} = \frac{1}{T_\mathrm{P}} + \frac{1}{T_\mathrm{R}}. \tag{27}$$

allows to simplify eq. (25) considerably:

$$\left(\frac{\mathrm{d}n}{\mathrm{d}t}\right)_{\text{orientation}} = \frac{N}{T_\mathrm{P}} - \frac{n}{\tau}. \tag{28}$$

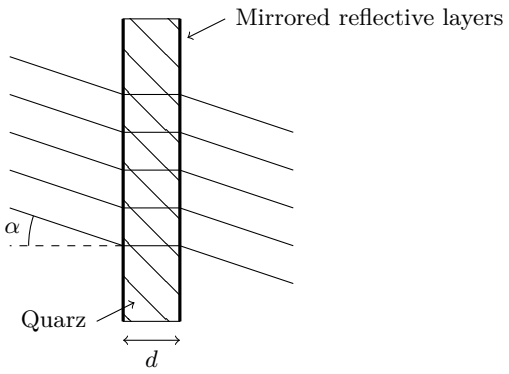

Figure 5: Schematic representation of the etalon used in the experiment.

Setting $n(0) = n_0$, we can immediately solve the initial value problem with

$$n(t) = (n_0 - n_{\max}) \exp\left(-\frac{t}{\tau}\right) + n_{\max}. \tag{29}$$

Under the assumption that the pumping starts when statistical equilibrium is in place, i. e. $n_0 = 0$, the solution becomes

$$n(t) = n_{\max}\left(1 - \exp\left(-\frac{t}{\tau}\right)\right). \tag{30}$$

2.4. Elements in the optical path

In the following we summarize some of the elements that are part of the optical path at various points in the experiment.

Fabry-Perot Etalon The etalon consists of a piece of quarz glass which is coated with mirrored reflective layers on its front- and backside. The basic principle of an etalon is sketched in fig. 5. Light enters from the left side and gets partially reflected and partially transmitted at the mirrored layer on the right side. A portion of the reflected light gets reflected again at the reflective mirrored layer on the left and interferes with the light that was originally transmitted through the right side. Whether light of a specific wavelength interferes with itself constructively or destructively depends on the thickness d of the material. The transmission of light is also very dependent on the incident angle α; the wavelength of the m-th transmission maximum is at

$$\lambda_m = \frac{2d}{m}\sqrt{n^2 - \sin^2\alpha}, \tag{31}$$

where n is the refractive index of the etalon material. The distance of two neighbouring maxima is called the free spectral range and is given by

$$\mathrm{FSR} = \frac{c}{2nd} \tag{32}$$

for the case $\alpha = 0$. In our experiment, the free spectral range is $\mathrm{FSR} = (9924 \pm 30)\,\mathrm{MHz}$.

λ/4-plate A $\lambda/4$-plate is made out of a birefringent material; i. e. a material whose index of refraction differs for perpendicular crystal axes. The two polarization axes of linearly polarized light that enters a $\lambda/4$-plate will traverse the material at different velocities which means that both polarizations will experience a shift in phase when exiting the plate. If the plate's thickness is chosen carefully (and with respect to the wavelength of the incident light; hence the name $\lambda/4$), the phase shift is exactly $\frac{\pi}{4}$ such that the initially linearly polarized light is now circularly polarized. Of course, if the wavelength and the thickness do not fit together, the resulting light is not always circularly polarized but elliptically polarized in general.

Diode laser The source for the light used for the optical pumping process is given by a a double-hetero-structure GaAlAs laser diode. The advantage of that choice of laser lies in the linear polarizatino of the light and an extremely narrow frequency band; however, the light emitted is extremely divergent which is why it is important to adjust the beam path with lenses as precise as possible. The diode itself consists of a p-n-junction where electrons and holes can recombine in the boundary region. The energy difference can be released as light. Due to the recombination of electrons and holes in the boundary region, the local charge density becomes negative in the p-zone and positive in the n-zone. The resulting electric field inhibits the recombination process and bends the valence- and conduction bands of the semiconductor such that the fermi energies of the negative and the positive zones get shifted. Both electrons and holes can then coexist in a narrow corridor which makes way for a region where population inversion is possible after application of a forward current.

3. Setup and Procedure

3.1. Setup

The core of the setup is the optical bench at which the diode lase is mounted. The laser is immediately followed by a lens (focal length of $\approx 50\,\text{mm}$) to focus its divergent beam. Afterwards, there is the possibility to mount different elements such as the $\lambda/4$-plate, a linear polarizer, various neutral density filters or the chopper, depending on the part of the experiment. This is followed by the mounting of the glass cell with the Rubidium vapour. Four different Helmholtz coil pairs are fixed at the mounting of the glass cell and a fifth coil pair as well as an radio-frequency transmitter is mounted directly at the glass cell itself. A second lens (focal length of $\approx 150\,\text{mm}$) is mounted after the cell which focusses the light at the photo diode which is mounted at the end of the optical path A sketch of this setup can be seen in fig. 6.

The different components named above can be operated separately. The laser is cooled by Peltier unit with which the temperature of the laser can be controlled to 0.1 K. The diode current controller can be used to set different currents for the laser or, alternatively, an additional function generator can be used to modulate the laser with a sawtooth signal for example. To detect the photo diode's signal the output of the laser diode is connected over an amplifier with an oscilloscope. Coils 1, 2, 3, and 5 are positioned in such a way that the magnetic fields they induce are parallel (or anti-parallel) to the laser beam while coil 4 is positioned such that the magnetic field is in vertical direction, that is, perpendicular to the ground. The coils themselves differ in their inductance: Coils 1 and 4 are used to create constant magnetic fields with adjustable field strength while the other coils are operated with frequency generators creating sinusoidal or rectangular pulses. The RF-transmitter is also operated with a frequency generator which can send out sinusoidal pulses. The actual settings used differ from part to part during the experiment.

3.2. Procedure

During the performance of the experiment the different subtasks which are explained in the following were not performed in the same order as presented. On the contrary, some of the subtasks were performed multiple times with varying degrees of success on different days.

3.2.1. Characterisation of the laser diode

First, with just lenses and the etalon mounted between laser and PD, the laser was operated with a sawtooth signal. To be able to see the transmission peaks of the etalon it is important that it is set in such a way that the laser beam enters it perpendicular to the surface. After the etalon is adjusted in this way the position and orientation of the lenses can be adjusted so the transmission peaks become maximal. After the beam path was optimized, the temperature was set to different values to study its influence; measurements of the signal for such different temperatures can be found in the appendix

(cf. fig. 23). As the influence of the temperature was studied, the temperature was set to 34.6 °C for the whole experiment. Next, the laser current was studied for different values with constant temperature which shows a similar but overall weaker influence on the signal. The change of the current could be seen in a drift of the etalon peaks.

3.2.2. Spectroscopy of the hyperfine structure

The goal of this task is to measure the hyperfine structure of the Rubidium isotopes. For this, the etalon was removed and the glass cell was mounted at the optical bench. The laser was operated with a sawtooth signal again and at the oscilloscope one could see the absorption spectrum of the hyperfine structure. The settings of the laser current were adjusted to optimize the measured spectrum. Further, the glass cell was regularly heated using a hair dryer to increase the pressure in the cell. As expected, we could only see six of the theoretically eight distinct spectral lines: four of the six lines observed were clearly recognizable and two of them were rather hard to find. To be able to analyze the measured spectra afterwards and determine the hyperfine constants we also did calibration measurements: To this end, the glass cell was removed and the etalon was put back on the optical bench. For the same laser settings used for the spectrum measurement the transmission maxima of the etalon were measured to be able to recalculate the time axis of the oscilloscope into a frequency axis.

3.2.3. Double resonance

In the next subtask double resonance is used to determine the nuclear spins of both Rubidium isotopes. For that, the $\lambda/4$-plate the quarter wave plate is mounted behind the first lens without the glass cell or etalon in the optical path. To be able to set the $\lambda/4$-plate in such a way that it truly generates circularly polarized light from the laser a linear polarizer is mounted behind the $\lambda/4$-plate. Then, the laser was operated with ramp signal so a change of the intensity could be seen quite nicely on the oscilloscope, while different setting of the quarter wave plate were tested by rotating the linear polarizer. If the light after the $\lambda/4$-plate is truly circularly polarized, a rotation in the linear polarizer should not result in a change of intensity. We were, however, not able to find a setting of the $\lambda/4$-plate for which the intensity did not change at all but instead found a setting for which variation in the intensity was minimized.

After the $\lambda/4$-plate was set, the linear polarizer was removed and the glass cell was inserted into its mounting again. After that, coil 2 was operated with a sinusoidal modulation and the RF transmitter was operated with a frequency of $\nu_{\mathrm{RF}} = 500\,\mathrm{kHz}$. Using this settings, the laser current was used in a constant current mode. The current was changed until optical pumping occurs. To increase the chance of success for this search it proved useful to set the coil 2 two a high amplitude. Two values for the laser current were found that maximized the absorption, each current belonging to one of the isotopes. It is important to note that the laser currents for which optical pumping occurs changed noticeably over the days. On the first day they were found to be 64.4 mA and 64.8 mA at the second day they shift slightly but at the third day they were found to

be at 67.8 mA and 68.2 mA. Since the laser must be also set to these exact currents in the following subtasks, this identification of the right currents for optical pumping was redone a couple of times to adjust to the changed values.

With the right laser current settings found, coil 1 was supplied with a constant current which was set to a value for which the absorption peaks are equidistantly spaced. To find this value the amplitude of coil 2 was decreased as this led to less noisy signals and more defined peaks rather than a detailed spectrum. Surprisingly the peaks were equidistant without any current in coil 1, but this setting is not the one needed to calculate the nuclear spin. While the current of coil 1 was increased, the peaks got less equidistant at first but became equidistant again at some point, the exact current was noted. After the right value was found an additional coil was turned on. Coil 4 was also operated with a constant current. This current was set such that the absorption peaks became maximal, which indicates that the magnetic field of coil 4 should compensate the vertical stray field. After coil 4 was set, coil 1 was operated with reversed polarity and the now changed setting for which the peaks are equidistant were determined. With the different currents of coil 1 for each polarisation the horizontal stray field and the nuclear spin can be calculated while the setting of coil 4 can be used to calculate the vertical magnetic field. It should be noted that there was more of a range of currents in coil 1 for which the peaks were more or less equidistant. Further, noise of the signal made it hard to find the best spot. This measurement was done for both laser current settings found at the beginning; the currents measured can be found in table 5 and the measured photo diode signal for each setting can be found in fig. 22 in the appendix.

The first time this part of the experiment was done while the experimental setup was not specially orientated but just aligned to the wall of the room, which was a more or less in the north east direction. The experiment was redone while the longitudinal direction of the experiment pointed to the north, so that the horizontal stray field measured can be compared to the horizontal magnetic field of the earth. Surprisingly, this reorientation did not change the settings of coil 1 which still yielded equidistant absorption peaks.

3.2.4. Spin precession

In principal the setup is similar to the one for the double resonance; however the RF transmitter is not used and the coils used are coil 1 and coil 5. Coil 1 is set in such a way that it compensates the horizontal stray field – the value for this is know from the double resonance part – and coil 5 is turned on and off with periodically using a rectangular pulse supplied by an external frequency generator. Coil 5 is used specifically because of its low inductance since the magnetic field should be turned of quite rapidly to obtain a good spin precession signal. Again, we attempted to get better signals by heating the cell from time to time using the hair dryer.

For this part of the experiment we were not able to find a signal for the most time, but with coil 1 turned off and coil 4 set to the value from the double resonance task the spin precession could be observed. At the end of the experiment we finally were able to also measure some spin precession signal while coil 4 was turned off and coil 1 was set to different currents. Finally, to be able analyze data for this subtask we measured the

spin precession for different currents for coil 1 and 4 and different orientations of the experimental set up with respect to the magnetic field.

3.2.5. Relaxation time: Dehmelt's method

This subtask has the goal to determine the relaxation time of the pumped cell using the Dehmelt method. For this task, coil 3 is operated with a longitudinal oscillating signal and coil 4 is set such that the vertical stray field is compensated. If the laser current is set in such a way that optical pumping can occur, one should see a rapid loss of intensity directly after the magnetic field of coil 3 changed and afterwards an exponential increase of the intensity. This exponential increase is recorded at the oscilloscope while different neutral density filter are mounted between the $\lambda/4$-plate and the glass cell. Again, the cell was heated before the measurements.

In addition, the intensity filters were calibrated by measuring the intensity of the laser modulated by a ramp signal, for the different filters and without any filter for the same laser settings. For this measurements the cell was removed.

3.2.6. Relaxation time: Franzen's method

Again the relaxation time will be determined, this time using Franzen's method. For this method, the chopper is mounted between the $\lambda/4$-plate and the cell. Without any magnetic field induced by any of the coils the laser is set such that absorption can be observed and is at its maximum. For different chopper speeds the signal of the photo diode is measured. Again the cell was heated for the measurements to increase the pressure.

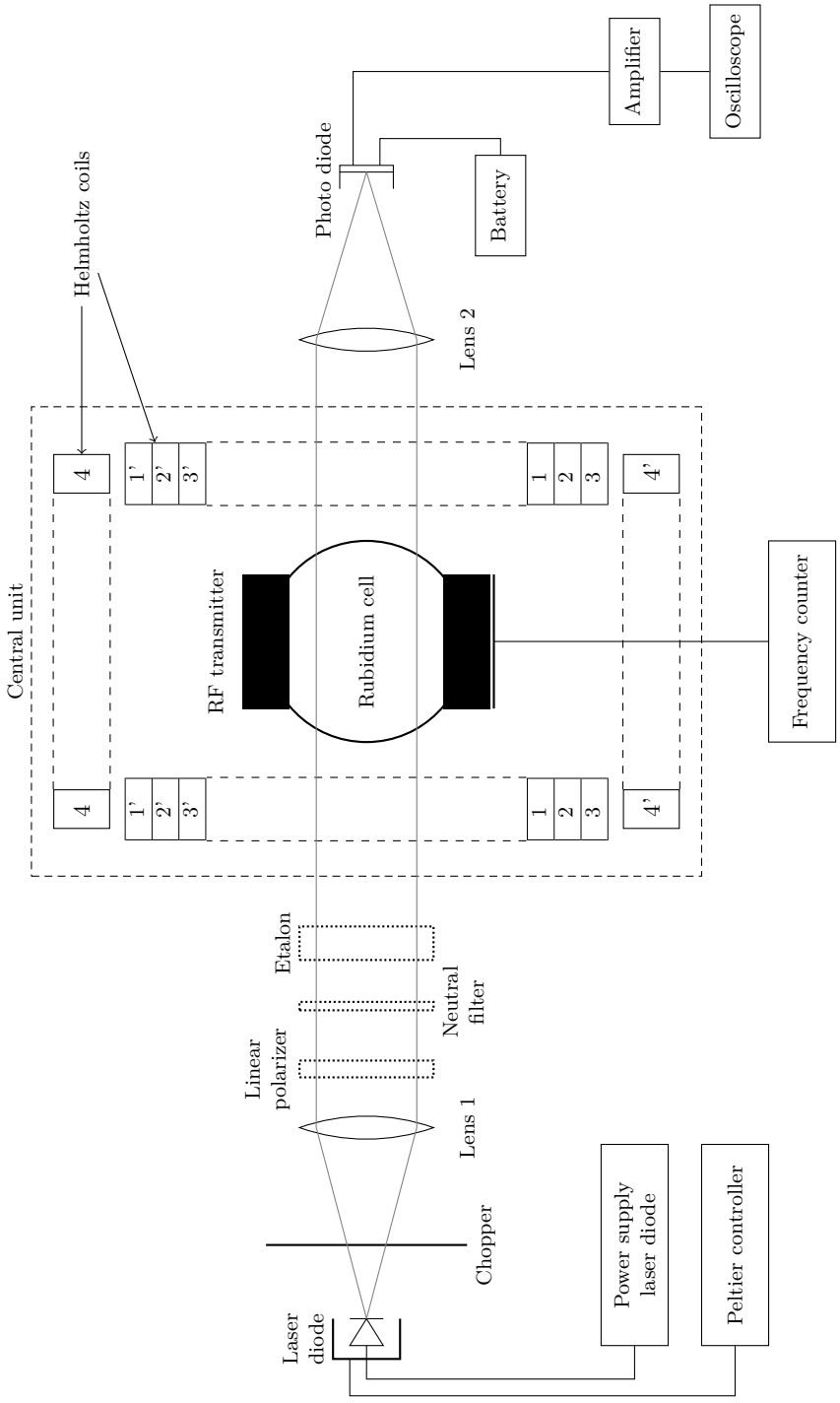

Figure 6: A schematic representation of the setup used in the experiment. The dashed optical elements refer to elements that are placed in the optical path at various points in the experiment. Adapted from the Staatsexamen [1].

4. Analysis

4.1. Spectroscopy of the hyperfine structure of Rubidium

For the investigation of the hyperfine structure of Rubidium, we proceed in three steps: First, we analyze the calibration of the triangle voltage (in the following referred to as voltage ramp) using the etalon. Then, we use this calibration to calculate the frequency shifts of the transition energies from the D_1 line whose location we will approximate, too. Lastly, we use the frequency shifts to calculate the hyperfine structure constants of ^{85}Rb and ^{87}Rb.

4.1.1. Time-Frequency calibration using the Etalon

After setting up the spectroscopy-specific part of the experiment and connected a voltage ramp to the laser as described in section 3.2.2, the etalon was inserted in the optical path and the resulting spectrum was recorded; it can be seen in fig. 7 alongside the ramp voltage which was used to trigger the oscilloscope. The known free spectral range of the etalon can now be used to convert "distances" on the time axis into frequency differences of the laser light. For that, we search for neighboring resonant interference peaks on the etalon spectrum which are on the same ramp section. Figure 7 shows three groups of peaks with two peaks in each group. The time of each peak alongside its error was calculated via visual inspection. The absolute time of each peak can be seen in table 2 along with the difference $\Delta t = t_{\text{Right}} - t_{\text{Left}}$ of two adjacent peaks. The weighted mean of these time differences can be calculated to be

$$\Delta t = (1.18 \pm 0.03)\,\text{ms}, \tag{33}$$

where the error was propagated using Gaussian error propagation.

Now, we know that the difference in the frequency of the laser light should correspond to the free spectral range of the etalon, namely $\text{FSR} = (9.924 \pm 0.030)\,\text{GHz}$. Multiplication of time differences with the conversion factor $\eta = \text{FSR}/\Delta t$ thus results in a difference in frequency of the laser light, under the condition that the points in time whose difference is to be measured are on a connected section of the ramp and the ramp is traversed with the same frequency and the same amplitude. Calculating the conversion factor with the free spectral range and the weighted mean of the time differences of

Table 2: Location (on the time axis) of each pair of peaks in the etalon spectrum (cf. fig. 7) with their difference.

Ramp section	t_{Left} [ms]	t_{Right} [ms]	Δt [ms]
Descending 1	2.02± 0.03	3.13± 0.04	1.11± 0.05
Ascending	5.50± 0.05	7.04± 0.04	1.54± 0.06
Descending 2	8.64± 0.03	9.75± 0.02	1.11± 0.04

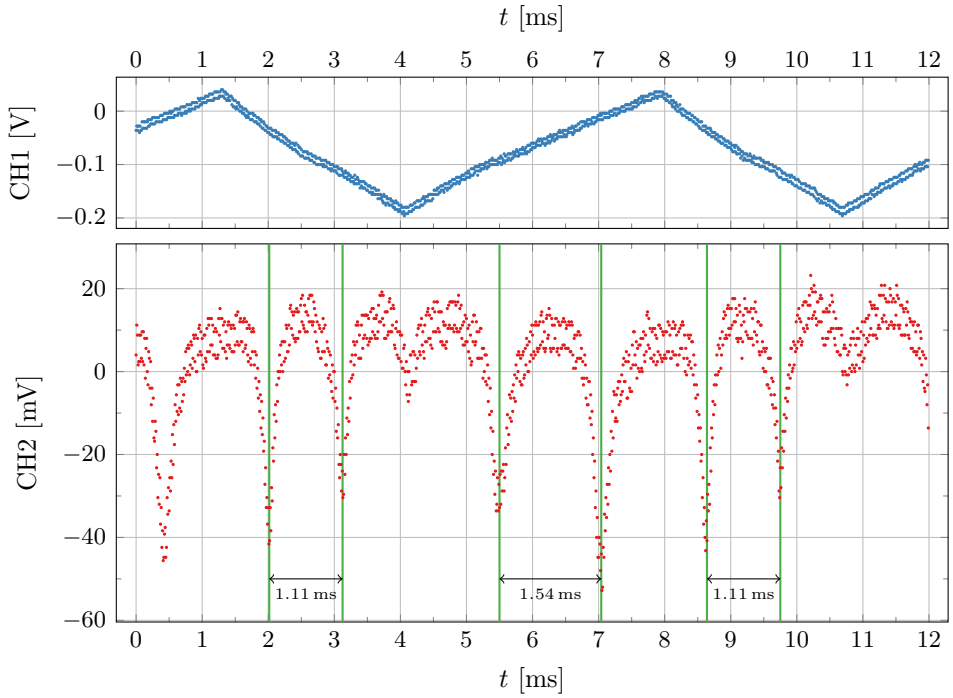

Figure 7: Spectrum of the etalon used for the calibration of the time axis for the hyperfine structure spectroscopy. The plot above shows the ramp voltage and the plot below shows the inverted signal recorded by the photo diode.

the last paragraph gives

$$\eta = \frac{\mathrm{FSR}}{\Delta t} = (8.38 \pm 0.19) \times 10^3\,\mathrm{GHz\,s^{-1}}. \tag{34}$$

4.1.2. Frequency shifts

The recorded hyperfine spectrum of Rubidium can be seen in figs. 8 and 9. The voltage of the ramp is decreasing in time for the first figure and increasing for the second figure. The location of the absorption peaks and their errors was, again, determined visually and marked in the plot shown in figs. 8 and 9 in green lines. The light green shading indicates the uncertainty in the peak location. As one can see in the plot, peaks swallowed by larger peaks (such as the second peak from the left in fig. 8) which are barely visible, were assigned a location with a greater uncertainty than the more well-defined peaks. Based on the theoretical transition frequencies depicted in fig. 2 the absorption peaks were labeled which can also be seen in both plots (due to the limited space in the figure, the transitions were abbreviated, i. e. $^{87}\mathrm{Rb}_{2\to1}$ stands for $^{87}\mathrm{Rb}, F\colon 2 \to 1$). As expected, we did not manage to capture all expected eight transitions, but only six of them. As the theoretical value for the transition energies of the ^{85}Rb-transitions $3 \to 2$ and $3 \to 3$ as well as $2 \to 2$ and $2 \to 3$ are closest to each other and their general position fits to

the two largest peaks in the spectrum, we assigned them to these positions.

Table 3: Frequency shifts of the absorption spectrum taken with an descending ramp (cf. fig. 8).

Line name	Absolute peak time t [ms]	Δf [GHz]	Δf (lit.) [GHz]
^{87}Rb, $F\colon 1 \to 2$	1.004± 0.010	4.68± 0.14	4.58
^{87}Rb, $F\colon 1 \to 1$	0.915± 0.015	3.93± 0.16	3.76
^{85}Rb, $F\colon 2 \to 2/3$	0.669± 0.005	1.87± 0.07	1.74
^{85}Rb, $F\colon 3 \to 2/3$	0.260± 0.007	−1.55± 0.08	−1.30
^{87}Rb, $F\colon 2 \to 2$	0.171± 0.015	−2.30± 0.14	−2.25
^{87}Rb, $F\colon 2 \to 1$	0.082± 0.005	−3.04± 0.09	−3.07

Table 4: Frequency shifts of the absorption spectrum taken with an ascending ramp (cf. fig. 9).

Line name	Absolute peak time t [ms]	Δf [GHz]	Δf (lit.) [GHz]
^{87}Rb, $F\colon 1 \to 2$	0.659± 0.005	6.17± 0.15	4.58
^{87}Rb, $F\colon 1 \to 1$	0.76 ± 0.02	5.26± 0.20	3.76
^{85}Rb, $F\colon 2 \to 2/3$	1.138± 0.015	2.15± 0.14	1.74
^{85}Rb, $F\colon 3 \to 2/3$	1.648± 0.010	−2.11± 0.10	−1.30
^{87}Rb, $F\colon 2 \to 2$	1.73 ± 0.02	−2.83± 0.18	−2.25
^{87}Rb, $F\colon 2 \to 1$	1.861± 0.010	−3.90± 0.13	−3.07

Now, using the theoretical values for the shifts of the transition energy with respect to the D_1 line, we were able to reconstruct the position of the D_1 line using the conversion factor: For the time-location t_i of each absorption peak i we subtracted the frequency shift Δf_i known from theory divided by the conversion factor η to obtain the absolute time-position $(t_{D_1})_i$ of the D_1-line:

$$(t_{D_1})_i = t_i + \frac{\Delta f_i}{\eta}, \qquad \sigma_{(t_{D_1})_i} = \sqrt{\sigma_{t_i}^2 + \left(\frac{\Delta f_i}{\eta^2} \cdot \sigma_\eta\right)^2}. \tag{35}$$

It should be noted that the literature values of the two peaks we couldn't clearly resolve and which are "merged" into one peak were averaged so that we can proceed with six effective transitions. Taking the weighted mean of the set of $(t_{D_1})_i$'s gives us our approximation of the D_1 line as shown in figs. 8 and 9[1]. This gives

$$(t_{D_1})_{\text{Desc.}} = (4.46 \pm 0.04) \times 10^{-4}\,\text{s}, \tag{36}$$

$$(t_{D_1})_{\text{Asc.}} = (1.395 \pm 0.006) \times 10^{-3}\,\text{s} \tag{37}$$

for the plots with descending and ascending ramp, respectively. Having obtained the time-position of the D_1-line, the frequency shifts of each transition can be calculated by

[1] Of course, the weighted mean was calculated for each of the two plots seperately

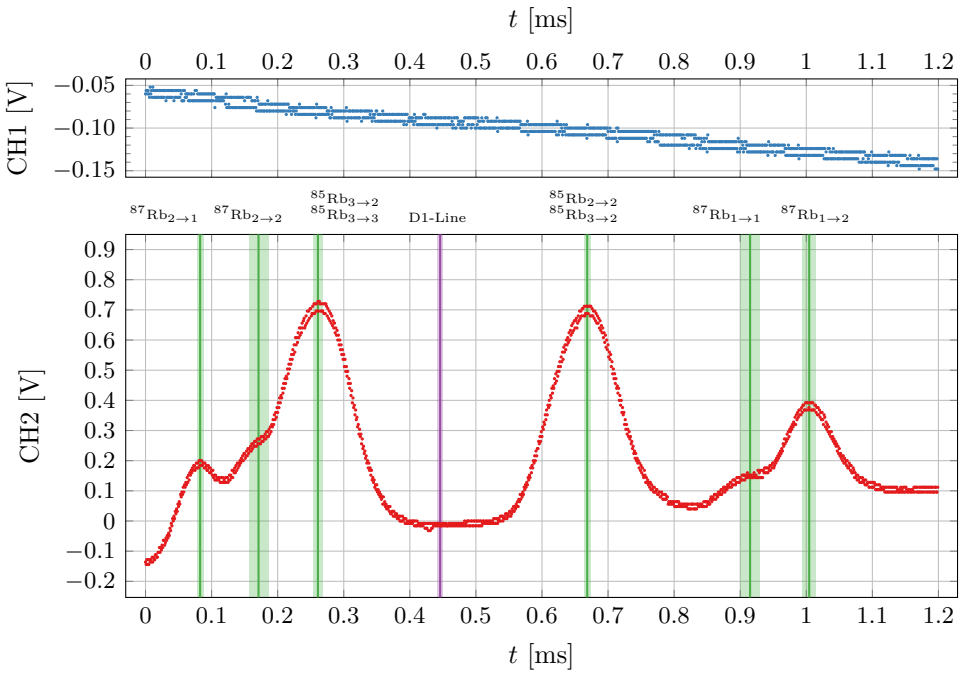

Figure 8: Hyperfine spectrum of Rubidium as recorded with the photo diode. The descending ramp used to modulate the laser light is shown above the main plot.

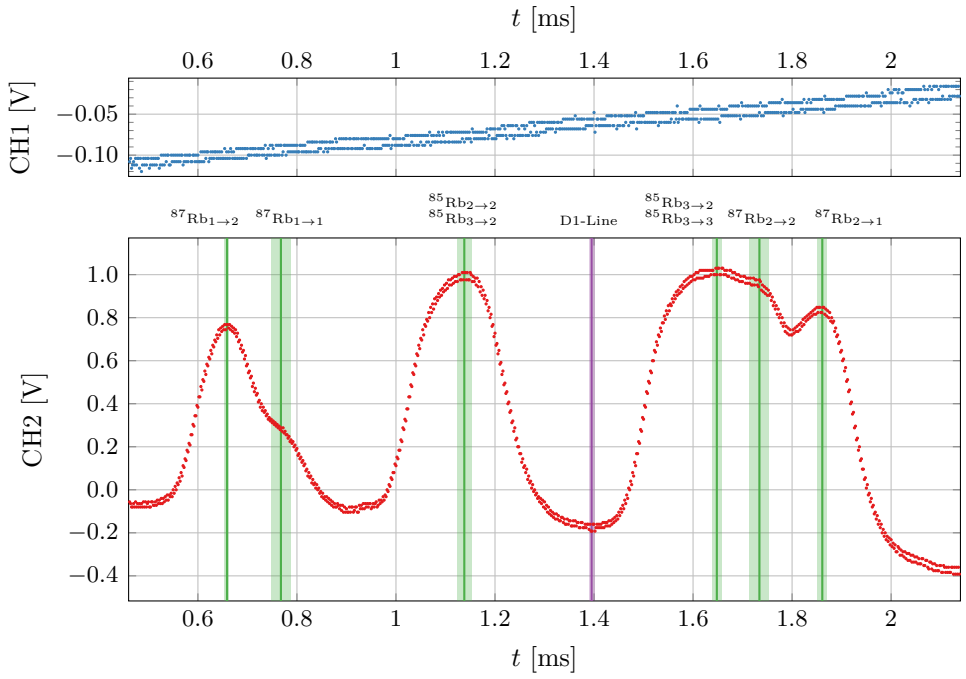

Figure 9: Hyperfine spectrum of Rubidium as recorded with the photo diode. The ascending ramp used to modulate the laser light is shown above the main plot.

determining the time-distance between each peak and the D_1 line and multiplying that time difference with the conversion factor η. For the ith peak at time t_i this gives

$$\Delta f_i = \eta \cdot (t_i - t_{D_1}), \qquad \sigma_{\Delta f_i} = \sqrt{(\sigma_\eta \cdot (t_i - t_{D_1}))^2 + (\eta \cdot \sigma_{t_i})^2 + \left(\eta \cdot \sigma_{t_{D_1}}\right)^2}. \tag{38}$$

The results for the descending and the ascending ramps are shown in tables 3 and 4, respectively, alongside the literature value of the frequency shift.

As one can see from table 3, the calculated frequency shift of each line fits the frequency shift from the literature quite well, differing by 2-σ at most. By constrast, thee results of the absorption spectrum with ascending ramp given in table 4 differ quite a lot from their literature values, with deviations of about 8-σ. Because of this, we will restrict ourselves to the results from table 3 for the following calculations. A discussion of this great discrepancy between the two related measurements follows in section 5.4.

4.1.3. Hyperfine structure constants

Based on the results shown in table 3, we can proceed to calculate the hyperfine structure constants. For each level (for us, the levels are given by the $^2\mathrm{S}_{1/2}$ and $^2\mathrm{P}_{1/2}$ states of Rubidium), the hyperfine structure constant A can be calculated by

$$A = \frac{h\Delta\nu}{F+1} \tag{39}$$

where $\Delta\nu$ is the frequency difference of two adjacent hyperfine structure states and F refers to the minimum of the F-quantum number of both of these states. We can use the frequency shifts determined in the last section to calculate the frequency difference $\Delta\nu$ of two adjacent states by considering the difference of two neighboring transitions, i. e. a pair of transitions that either share initial states and the final states are neighboring or vice-versa.

First, we focus on ^{87}Rb. For the $^2\mathrm{S}_{1/2}$ level, we two pairs of neighboring transitions at our disposal, namely the pair $^{87}\mathrm{Rb}, F\colon 1 \to 2$ and $^{87}\mathrm{Rb}, F\colon 2 \to 2$ as well as the pair $^{87}\mathrm{Rb}, F\colon 1 \to 1$ and $^{87}\mathrm{Rb}, F\colon 2 \to 1$. Substituting $\Delta\nu$ in eq. (39) for the difference of the frequency shifts of each pair and letting $F = 1$ (this is the minimum F-quantum number in the differing states for both pairs) gives us two hyperfine structure constants,

$$(3.5 \pm 0.1)\,\mathrm{GHz}, \quad \text{and} \quad (3.49 \pm 0.09)\,\mathrm{GHz}. \tag{40}$$

The error on both values was constructed via Gaussian error propagation. Taking the weighted mean and multiplying by h to obtain electronvolts we arrive at

$$A_{^{87}\mathrm{Rb},^2\mathrm{S}_{1/2}} = (3.49 \pm 0.07)\,\mathrm{GHz} = (1.44 \pm 0.03) \times 10^{-5}\,\mathrm{eV}. \tag{41}$$

Again, the error was propagated using Gaussian error propagation. For the $^2\mathrm{P}_{1/2}$ level, we proceed in exactly the same way. Again, we have two pairs of neighboring transitions at hand, namely the pair $^{87}\mathrm{Rb}, F\colon 1 \to 1$ and $^{87}\mathrm{Rb}, F\colon 1 \to 2$ and the pair $^{87}\mathrm{Rb}, F\colon 2 \to$

Table 5: The results of the measurement with north orientation, no current in coil 1 and different currents in coil 4.

Isotope	I_4 [mA]	$I_{1,1}$ [mA]	$I_{1,2}$ [mA]
^{85}Rb	71± 1	139± 2	132± 2
^{87}Rb	71± 1	93± 2	86± 2

1 and $^{87}\mathrm{Rb}, F\colon 2 \to 2$. Calculating the difference of the frequency shifts of the transitions in each pair gives us a frequency shift $\Delta\nu$. Using eq. (39) with $F = 1$ then gives

$$(0.38 \pm 0.10)\,\mathrm{GHz}, \quad \text{and} \quad (0.37 \pm 0.08)\,\mathrm{GHz}. \tag{42}$$

Again, taking the weighted mean then gives

$$A_{^{87}\mathrm{Rb},^2\mathrm{P}_{1/2}} = (0.37 \pm 0.07)\,\mathrm{GHz} = (1.54 \pm 0.27) \times 10^{-6}\,\mathrm{eV}. \tag{43}$$

Now, we focus on ^{85}Rb. Unfortunately we weren't able to clearly distinguish between the relevant peaks for the transitions of ^{85}Rb. The energy difference can thus only be approximated roughly and only one of the two relevant hyperfine structure constants can be calculated. We will focus on the $^2\mathrm{S}_{1/2}$ structure constant in the following. For that, we consider the pair of neighboring transitions consisting of $^{85}\mathrm{Rb}, F\colon 2 \to 2$ and $^{85}\mathrm{Rb}, F\colon 3 \to 2$. Here, $F = 2$ as it is the minimum of the F-quantum number of both transitions. Substituting the difference of both transitions for $\Delta\nu$ in eq. (39) gives

$$A_{^{85}\mathrm{Rb},^2\mathrm{S}_{1/2}} = (1.14 \pm 0.08)\,\mathrm{GHz} = (4.71 \pm 0.15) \times 10^{-6}\,\mathrm{eV}. \tag{44}$$

4.2. Double resonance

As described in section 3.2.3 we determined the currents in coil one to get equidistant peaks for both polarities and both isotopes and also the current for coil four for maximized peaks. The values we measured are given in table 5. From the current set in coil 4 the magnetic field it created can be calculated, which should be equal to the vertical stray field. Using table 1 in [3] the magnetic field induced by coil 4 was calculated and the error was propagated with

$$\sigma_{B_i} = \sqrt{\left(\left(\frac{B}{I}\right)_i \cdot \sigma_I\right)^2 + (I \cdot (0.01 \times 10^{-4}\,\mathrm{T\,A^{-1}}))^2}, \tag{45}$$

where $(B/I)_i$ was extracted from the table. As result we have got

$$B_{\mathrm{vert}} = (33.8 \pm 0.5)\,\mu\mathrm{T}. \tag{46}$$

For the horizontal fields the same method can be used to calculate the magnetic fields induced by coil 1 for the two different polarities, the horizontal stray field is half of the difference of this two field, for which we got

$$B_{\mathrm{hor}} = (5.6 \pm 1.1)\,\mu\mathrm{T}, \tag{47}$$

where the error was propagated using Gaussian error propagation.

To be able to calculate the nuclear spin I of both isotopes one has to calculate the corrected magnetic field in horizontal direction with

$$B_{\text{corr}} = (7.99 \times 10^{-4}\,\text{T}\,\text{A}^{-1}) \cdot \frac{I_1 + I_2}{2}. \tag{48}$$

For the two isotopes we calculated

$$B_{\text{corr}}^{^{85}\text{Rb}} = (108.3 \pm 1.1)\,\mu\text{T}, \qquad B_{\text{corr}}^{^{87}\text{Rb}} = (71.5 \pm 1.1)\,\mu\text{T}. \tag{49}$$

So finally using eq. (19) the nuclear spins can be calculated, which yields

$$I_{^{85}\text{Rb}} = 2.51 \pm 0.03, \qquad I_{^{87}\text{Rb}} = 1.49 \pm 0.03. \tag{50}$$

The uncertainties for the corrected field were calculated as

$$\sigma_{B,\text{corr}} = \sqrt{\left(\frac{I_1 + I_2}{2}(0.01 \times 10^{-4}\,\text{T}\,\text{A}^{-1})\right)^2 + \left(\frac{7.99 \times 10^{-4}\,\text{T}\,\text{A}^{-1}}{2}\right)^2 \left(\sigma_{I_1}^2 + \sigma_{I_2}^2\right)} \tag{51}$$

and the uncertainties for the nuclear spins were calculated as

$$\sigma_I = \sqrt{\left(\frac{I}{\nu_{\text{RF}}}\sigma_{\nu_{\text{RF}}}\right)^2 + \left(\frac{I}{B_{\text{corr}}}\sigma_{B,\text{corr}}\right)^2} \tag{52}$$

where for the radio frequency we measured $\nu_{\text{RF}} = (503 \pm 3)\,\text{kHz}$.

4.3. Spin precession

In this subtask the magnetic stray field was measured using spin precession: The external horizontal field is compensated while a low-inductance coil is turned on and off again periodically. If the time needed for the magnetic field induced by the coils is lower than the precession time of the Rubidium ensemble, the polarization remains stationary and obtains an angular momentum in the external magnetic field of the earth. For the precession frequency it holds that

$$\nu = \frac{g_F \mu_{\text{B}}}{h} B_{\text{stray}}, \tag{53}$$

where B_{stray} is the remainder of earth's magnetic field. A calculation of B_{stray} is possible by measuring the precession frequency ν (or equivalently, the precession period $\tau = 1/\nu$) and rearranging the formula above to yield

$$B_{\text{stray}} = \frac{g_F \mu_{\text{B}}}{h}\nu = \frac{g_F \mu_{\text{B}}}{h}\frac{1}{\tau}. \tag{54}$$

The spin precession was measured as described in section 3.2.4. The measurements of the oscilloscope for different currents in coil 1 and 4 and therefore different induced magnetic field are of varying quality and tend to show a lot of noise; for example, the

measurement with north orientation and a current of 4 mA set to coil 1, which should compensate the horizontal magnetic stray field according to the double resonance measurement, is too noisy to determine the periods of the spin precession. The measurements with the experimental setup being orientated to the north and no current in coil four are shown in fig. 10. Plots of the other measurements can be found in the appendix (cf. figs. 19 to 21).

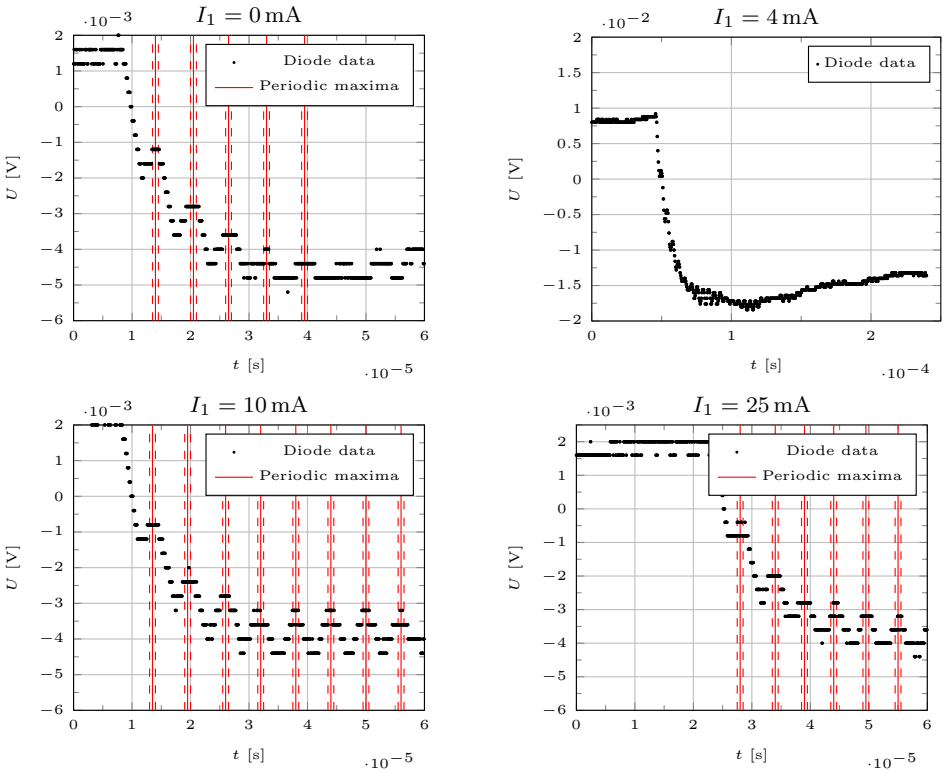

Figure 10: In this plots the measurements of the spin precession are shown with the current in coil four set to zero while the longitudinal axis of the experimental set up is directed to the north. The current in coil one differs from plot to plot with upper left 0 mA, upper right 4 mA, lower left 10 mA and lower right 25 mA.

As one can see in fig. 10, determining the period using fits does not seem suitable due to the noise in the data. Therefore the period was determined by identifying the maxima of the oscillation visually and calculating the period as the mean of the distance between two neighbouring maxima:

$$\tau = \frac{1}{n-1} \sum_{i=1}^{n-1} \left(t_{i+1}^{\max} - t_i^{\max} \right), \tag{55}$$

with n being the number of maxima identified and $t_i^{\max}$ being the position of the i^{th} maximum. The uncertainty for the positions of the maxima was estimated to be $\sigma_{t^{\max}} =$

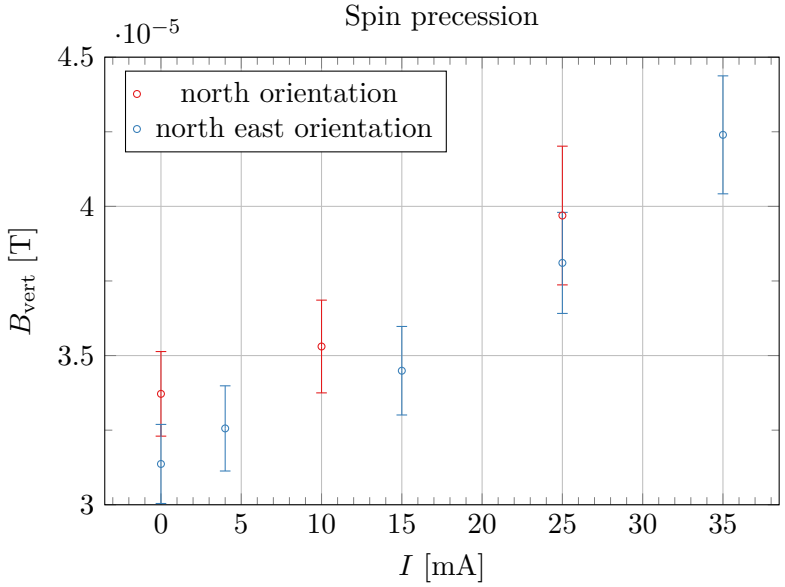

Figure 11: The calculated magnetic stray fields plotted over the horizontal magnetic field induced by coil one. In red the measurements with a north orientation are shown and in blue the ones with north east orientation. For all of the measurements the current in coil four was set to zero.

5×10^{-8} s which are also in the plots as dashed lines. With this the uncertainty of the period can be propagated to be

$$\sigma_\tau = \sqrt{\frac{2}{n-1} \cdot \sigma_{t^{\max}}}. \tag{56}$$

It was also considered to use the variance of the mean for the uncertainty of the period, but this led mostly to uncertainties to small that the propagation of the uncertainties was assumed to be more appropriate. Using the period the vertical magnetic field can be calculated with eq. (54) and the error can be propagated with

$$\sigma_{B_{\text{stray}}} = \frac{g_F \mu_{\text{B}}}{h} \frac{\sigma_\tau}{\tau^2}. \tag{57}$$

The calculated values for the magnetic field and the period for the different measurements can be seen in table 6,

In fig. 11 the magnetic stray fields measured for different horizontal magnetic fields induced by coil 1 are plotted. It can be seen that the magnetic stray field grows in the horizontal field induced by coil 1. Also the trend of the field seems to be similar for the north and north east orientations, but one could assume that the north east orientated data has an negative offset compared to the north orientated data. The stray field measured should be the vertical stray field when coil 1 just compensates the horizontal stray field. According to the double resonance experiment this should be at about 4 mA.

Table 6: The results of the spin precession measurement for various orientations of the setup.

Orientation	I_1 [mA]	I_2 [mA]	B_{stray} [µT]	τ [µs]
North	0± 1	0	33.7 ± 1.4	6.4± 0.3
	10± 1	0	35.3 ± 1.6	6.1± 0.2
	25± 1	0	40 ± 2	5.4± 0.3
East	0	71± 1	3.8 ± 0.2	56 ± 3
	0	71± 1	3.8 ± 0.2	56 ± 3
	0	71± 1	5.2 ± 0.5	36 ± 3
	0	71± 1	5.2 ± 0.5	36 ± 3
North-East	0± 1	0	31.4 ± 1.3	6.8± 0.3
	4± 1	0	32.6 ± 1.4	6.6± 0.3
	15± 1	0	34.5 ± 1.5	6.2± 0.3
	25± 1	0	38.1 ± 1.7	5.6± 0.3
	35± 1	0	42.4 ± 2.0	5.1± 0.2
	0	71± 1	4.1 ± 0.2	52 ± 3
	0	71± 1	5.4 ± 0.4	40 ± 3
	0	71± 1	3.3 ± 0.3	65 ± 5
	0	71± 1	5.9 ± 0.4	36 ± 3

As said before, the measurement with north orientation for this value is not usable but the one for the north east orientation is and gives us

$$B_{\text{stray}}(4\,\text{mA}) = (32.6 \pm 1.4)\,\mu\text{T}, \tag{58}$$

which is compatible with the result for the vertical stray field in section 4.2.

Also measurements with coil 1 turned off and the current of coil 4 set to 71 mA, such that its magnetic field compensates the vertical stray field, were done for north east and east orientation. The results of this measurements are to be found in table 6. For this measurements the uncertainty of the maxima is set to 5×10^{-7} s. Since the vertical stray field should be compensated the measured magnetic fields should represent the horizontal stray field. Thus, to be able to compare the spin precession measurements further with the double resonance measurements, the mean of the measured field was calculated for each orientation:

$$B_{\text{north-east}} = (4.7 \pm 0.3)\,\mu\text{T}, \qquad B_{\text{east}} = (4.9 \pm 0.4)\,\mu\text{T}, \tag{59}$$

the uncertainty was calculated with gaussian error propagation.

4.4. Relaxation time with Dehmelt's method

After the magnetic field is inverted, the difference in occupation numbers should obey the trend predicted in eq. (30). Further, it is reasonable to assume that the occupation number difference is proportional to the transmitted intensity I, i. e. $I(t) = I_{\text{min}} + \alpha n(t)$. This ultimately gives

$$I(t) = I_{\text{max}} - \Delta I \exp\left(-\frac{t}{\tau}\right). \tag{60}$$

where $I_{\max}$ is the intensity corresponding to a maximal difference in occupation numbers and ΔI is the difference between $I_{\max}$ and the intensity that is attained when the magnetic field reverses polarization. As the orientation time τ is related to the pumping time T_{P} and the relaxation time T_{R} via eq. (27) and the pumping time obeys $T_{\mathrm{P}} \propto I^{-1}$, we have

$$\frac{1}{\tau} = \frac{1}{T_{\mathrm{R}}} + \frac{1}{T_{\mathrm{P}}} \xrightarrow{I \to 0} \frac{1}{T_{\mathrm{R}}}. \tag{61}$$

Thus, in order to determine the true relaxation time T_{R} using Dehmelt's method, inverse orientation times $\frac{1}{\tau}$ are plotted against the intensity of the filters used to obtain that specific orientation time. For that, the intensity of the filters has to be obtained somehow. The calculation of the absorption of each filter is described in section 4.4.1. The section after that (section 4.4.2) then deals with the determination of the orientation time for each measurement and the extrapolation of the relaxation time T_{R}.

4.4.1. Calibration of the intensity filters

As described in section 3.2.5, a ramp voltage was applied to the laser diode and the Rubidium cell was removed from the optical path. Then, each filter was seperately placed inside the setup and the spectrum of the photo diode – which should follow the ramp voltage applied to the laser – was recorded. Our main idea is to compare the maximum intensity difference of each filter spectrum to that of the spectrum where no filter is in the optical path. Figure 12 shows the spectrum of the photodiode when no filter is in the optical path. The horizontal purple lines are positioned at the mean of the ten highest and ten lowest values, respectively. The error on the vertical position was determined by taking the standard deviation of those ten highest and lowest values and is shown shaded behind the purple lines. By taking the difference of these horizontal positions we obtain a quantity proportional to the intensity of the laser light. This quantity will be referred to as "absolute intensity" U^{abs} in the following paragraph.

The same measurements can be repeated for the other filters if the amplitude and frequency of the ramp is not altered in any way. By dividing the absolute intensity of each filter by the absolute intensity of the setup with no filter (which can be seen in fig. 12), we obtain the relative intensity I of each filter. For a filter i, the relative intensity I_i can thus be calculated as

$$I_i = \frac{U_i^{\mathrm{abs}}}{U_0^{\mathrm{abs}}}, \qquad \sigma_{I_i} = \sqrt{\left(\frac{\sigma_{U_i^{\mathrm{abs}}}}{U_0^{\mathrm{abs}}}\right)^2 + \left(\sigma_{U_0^{\mathrm{abs}}} \cdot \frac{U_i^{\mathrm{abs}}}{(U_0^{\mathrm{abs}})^2}\right)^2}. \tag{62}$$

Here, U_0^{abs} refers to the absolute intensity measured when there is no filter in the optical path. The absolute and relative intensities of each filter are displayed in table 10 alongside the label on each filter.

4.4.2. Orientation times

Now that the relative intensity of each filter is known, the orientation times τ of the orientation process of each filter has to be determined. We achieved that by fitting the

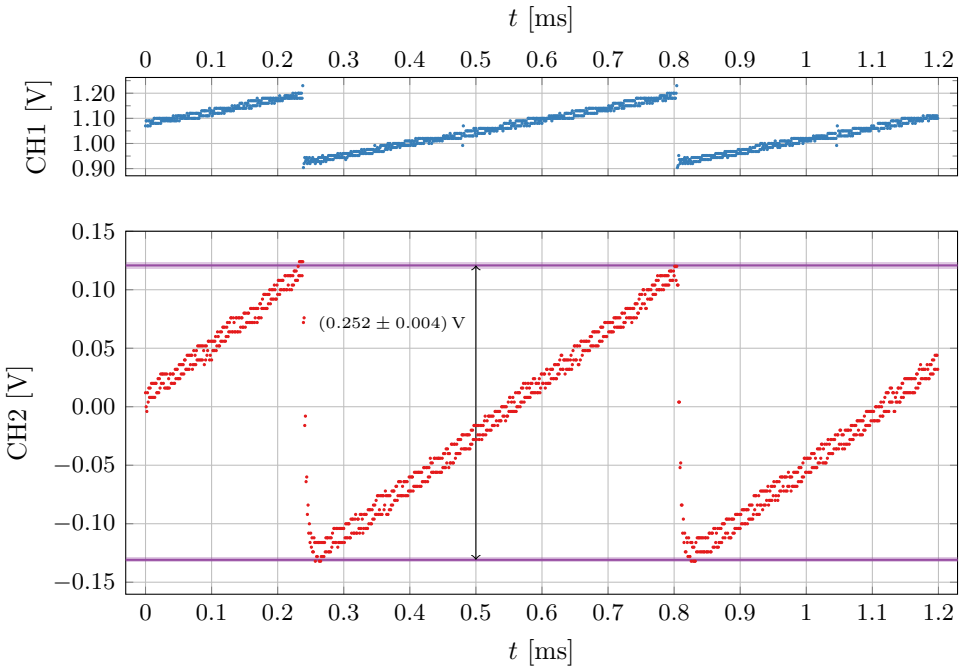

Figure 12: Signal recorded by the photo diode (CH2) when a ramp is applied to the laser and the optical path is clear. In purple: Mean of the largest and smallest 10 values, respectively.

Table 7: Orientation times τ with inverse τ^{-1} given for each filter for both isotopes ^{87}Rb and ^{85}Rb.

		^{85}Rb		^{87}Rb	
Filter	I	τ [ms]	τ^{-1} [MHz]	τ [ms]	τ^{-1} [MHz]
None	1	0.446± 0.005	2.240 ± 0.023	0.2406± 0.0019	4.16 ± 0.03
`d0_3`	0.506± 0.011	1.835± 0.012	0.545 ± 0.004	0.624 ± 0.010	1.602± 0.025
`d0_6`	0.431± 0.008	2.205± 0.008	0.4535± 0.0017	0.913 ± 0.015	1.094± 0.018
`d1_0`	0.210± 0.008	2.143± 0.013	0.4665± 0.0029	1.548 ± 0.008	0.646± 0.003
`d1_3`	0.134± 0.004	3.45 ± 0.09	0.290 ± 0.007	2.71 ± 0.14	0.370± 0.019
`d1_6`	0.159± 0.006	4.43 ± 0.14	0.226 ± 0.007	2.92 ± 0.12	0.342± 0.014
`d-0_37`	0.501± 0.011	1.565± 0.014	0.639 ± 0.006	0.536 ± 0.010	1.86 ± 0.03
`d-0_8`	0.215± 0.010	3.39 ± 0.08	0.295 ± 0.007	1.58 ± 0.04	0.632± 0.017

model

$$U(t) = U_{\max} - \Delta U \exp\left(\frac{t - t_{\text{off}}}{\tau}\right) \tag{63}$$

to the signal from the photo diode. In the formula above, $U_{\max}, \Delta U, t_{\text{off}}$ as well as the orientation time τ are fit parameters. For the fit itself we used the method `curve_fit` from the python package `scipy.optimize` [2]. The method was also supplied with the uncertainties on the voltage measurements, which was calculated by quadratically adding the error on the DC Gain and the vertical resolution of the oscilloscope as given in the manual of the oscilloscope [5]. The orientation times from the fit and their inverses are given in table 7 for each filter and for both isotopes. A visualization of the exponential saturation fits are shown collectively in the appendix in figs. 15 and 16 for both isotopes.

Now that the inverse orientation time τ^{-1} was calculated for various intensities, the inverse relaxation time T_{R}^{-1} can be extrapolated from the inverse orientation time as the intensity goes to zero. For that, we plot the inverse orientation time with respect to the relative filter intensity for both isotopes and perform a linear regression. Although we initially wanted to incorporate the uncertainty in I, we decided to neglect it as the uncertainty of the relative intensity σ_I takes the value 0 for the measurement without filter, making it difficult to weigh the results (assuming a quadratic loss function, one would have to divide by zero). Thus, the regression which was performed using R's linear model `lm` [4] was only supplied with the error on the τ^{-1}'s. The plot of the inverse orientation times can be seen in fig. 13 while the fit results themselves are given in table 8. That table also shows the t-statistic of each fit parameter and its quantile. Further, the residual standard error is given for both linear models. As the relaxation time's inverse T_{R}^{-1} can be extrapolated from τ^{-1} as the intensity goes to 0, the T_{R}^{-1} is

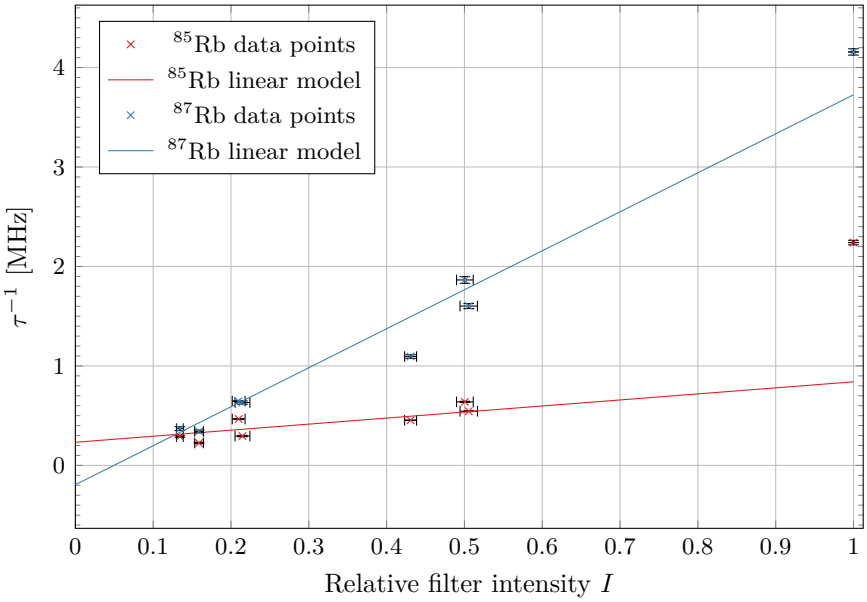

Figure 13: Inverse orientation times with respect to the relative intensity of each filter along with a linear regression.

Table 8: Fit results from the linear regression shown in fig. 13.

Isotope	Coefficient	Value [MHz]	t-value	p-value	χ^2/df
^{85}Rb	Intercept	0.23± 0.13	1.724	0.136	32.76
	Slope	0.6 ± 0.3	1.802	0.122	
^{87}Rb	Intercept	−0.19± 0.09	−2.101	0.08	11.69
	Slope	3.9 ± 0.4	10.479	4.43×10^{-5}	

given by the intercept of each linear model, giving

$$\frac{1}{T_{\mathrm{R}}^{^{85}\mathrm{Rb}}} = (0.23 \pm 0.13)\,\mathrm{MHz}. \tag{64}$$

$$\frac{1}{T_{\mathrm{R}}^{^{87}\mathrm{Rb}}} = (-0.19 \pm 0.09)\,\mathrm{MHz}, \tag{65}$$

Thus, the relaxation times of ^{85}Rb and ^{87}Rb are given by

$$T_{\mathrm{R}}^{^{85}\mathrm{Rb}} = (4.3 \pm 2.5)\,\mathrm{ms}, \tag{66}$$

$$T_{\mathrm{R}}^{^{87}\mathrm{Rb}} = (-5.1 \pm 2.4)\,\mathrm{ms}, \tag{67}$$

where the error was propagated via Gaussian error propagation.

4.5. Relaxation time with Franzen's method

In order to determine the true relaxation time T_R using Franzen's method, the Rubidium system is allowed to relax in the dark. The difference in occupation numbers then obeys eq. (24) as the only processes happening are relaxation processes. After a specific amount of dark time Δt that we have yet to determine, the system is exposed to the laser light again and the pumping begins again. For the intensity just at the dark time $I(\Delta t)$ it holds that

$$I(\Delta t) = I_\mathrm{max} + \Delta I \exp\left(-\frac{\Delta t}{T_\mathrm{R}}\right). \tag{68}$$

By determining the intensity just at the point where the light is switched on again and plotting it against the total time the system was in darkness, the relaxation time can be determined via an exponential fit.

Both the dark time and the position of the intensity was manually determined by a visual examination of the absorption spectrum. The exact intensity point was placed where the signal of the photo diode was transitioning in an exponential saturation. For each spectrum, this gives us a value for the intensity U^abs and a value for the time that intensity is attained, t_Right. Now, in order to determine the dark time of each spectrum, we extrapolated the other point in time with that same intensity t_Left in the region where the chopper starts blocking out the laser signal. The constructed intensities and time interval can be seen in the appendix in figs. 17 and 18 for various chopper speeds. While the error for the intensity can be calculated using the oscilloscope's specification as described in section 4.4.2, we estimated the uncertainty on both points in time to be about 10 time increments. The error on the dark time which is the difference between both points in time,

$$\Delta t = t_\mathrm{Right} - t_\mathrm{Left}, \tag{69}$$

can then be propagated via Gaussian error propagation. Lastly, the intensity value U^Abs is divided by the difference of the maximum and the minimum value of the spectrum so that the resulting intensity I is properly normalized. The results of the visual examination can be seen in table 9.

The next step is to plot the intensities against the dark times to find the relaxation time via an exponential fit. The visualization can be seen in fig. 14 which also shows a regression line where a model of the form

$$I(\Delta t) = A \cdot \exp\left(-\frac{\Delta t}{T_\mathrm{R}}\right) \tag{70}$$

is fitted against the data. In the formula above, A and T_R are fit parameters. The fit itself was performed using the `curve_fit` method of the python module `scipy.optimize`. We actively decided against an intensity offset as we had difficulties finding initial conditions so that the fit converges. The results are

$$A = 0.44 \pm 0.06, \tag{71}$$

$$T_\mathrm{R} = (8.5 \pm 2.5)\,\mathrm{ms}. \tag{72}$$

Additionally, to measure the goodness-of-fit, a residual standard error was calculated to be $\chi^2/\mathrm{df} = 2.08$.

Table 9: Dark times and relative intensities of the Franzen method to determine the relaxation time.

Measurement	Dark time Δt [ms]	Relative intensity I
1	12.50± 0.28	0.13 ± 0.07
2	9.07± 0.28	0.14 ± 0.04
3	6.65± 0.14	0.23 ± 0.03
4	5.34± 0.14	0.249± 0.028
5	4.47± 0.07	0.266± 0.026
6	3.76± 0.07	0.12 ± 0.05
7	3.31± 0.07	0.31 ± 0.03
8	2.96± 0.07	0.29 ± 0.03
9	2.67± 0.07	0.320± 0.027
10	2.49± 0.07	0.366± 0.022

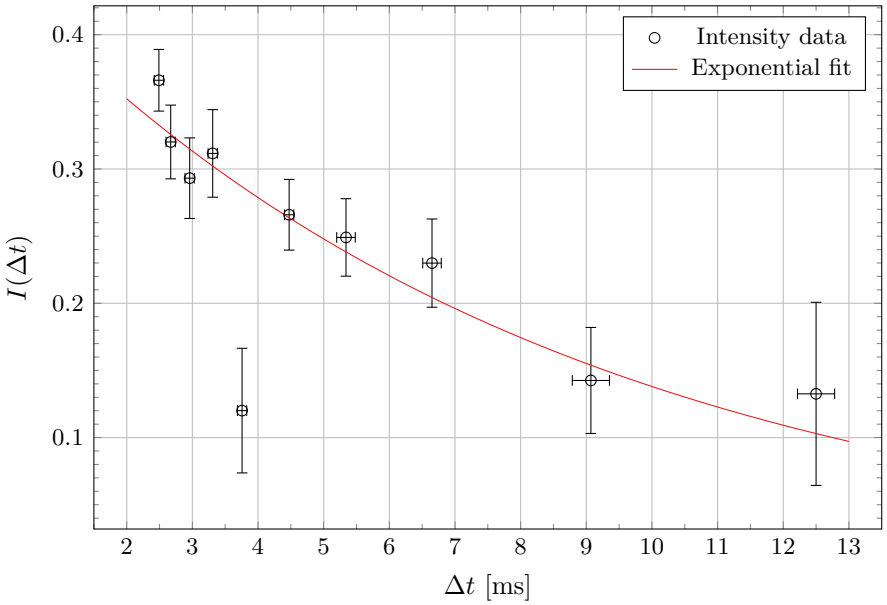

Figure 14: Exponential fit of the relative intensities with respect to the dark times in Franzen's method. The data can be found in table 9.

5. Discussion

5.1. Hyperfine spectrum spectroscopy

In the first part of the experiment, a triangle voltage was applied to the laser and the Rubidium cell was exposed to the laser light. The voltage was chosen in such a way that the hyperfine structure is visible on the signal of the photo diode recorded by the oscilloscope. Using a Fabry-Perot etalon, measurements were taken to calculate frequency differences from time differences given by the oscilloscope. Although we could only resolve six out of the expected eight spectral lines, the spectrum matches our expectation quite well for the case of the decreasing triangle voltage (see fig. 8 and table 3) with the theoretical frequency shifts deviating from the literature with 2-σ at most. In the case of the increasing triangle voltage, however, the results obtained do not look as great: table 4 shows a deviation as high as 8-σ from the literature values. Looking at the spectrum of the increasing triangle voltage (cf. fig. 9 also reveals that the spectrum itself is not only reversed to the one shown in fig. 8 (which is an effect we expect) but the peak location seems shifted and/or scaled. Our initial thought was that the triangle voltage was traversed with different speeds depending on whether the voltage is increasing or decreasing. However, by attempting to scale the conversion factor η we did not manage to obtain more consistent results. This can also be seen in the spectrum itself: By comparing the rightmost two green lines of fig. 8 with the leftmost two lines of fig. 9, one can see that they are roughly the same. The three green lines in the left of fig. 9, on the other hand, are more tightly bunched together than their counterpart in the case of the decreasing triangle voltage. This means that the issue lies deeper than a botched calculation of the conversion coefficient. As the effect is dependent on the direction of the triangle voltage we can rule out the possibility of mode jumps. A more promising explanation lies in a hysteresis-like effect in the laser diode. One possibility to investigate this issue further may be to traverse the triangle voltage at lower and lower speeds and examine the difference between the spectrum on the decreasing and increasing voltage at various speeds.

For the calculation of the hyperfine-structure constants we proceeded only with the data of the spectrum taken with the decreasing voltage ramp. As we managed to resolve only six out of the eight spectral lines, we managed to only calculate three out of the four relevant constants. Our results are

$$A_{^{87}\mathrm{Rb},^2\mathrm{S}_{1/2}} = (1.44 \pm 0.03) \times 10^{-5}\,\mathrm{eV}, \tag{73}$$

$$A_{^{87}\mathrm{Rb},^2\mathrm{P}_{1/2}} = (1.54 \pm 0.27) \times 10^{-6}\,\mathrm{eV}, \tag{74}$$

$$A_{^{85}\mathrm{Rb},^2\mathrm{S}_{1/2}} = (4.71 \pm 0.15) \times 10^{-6}\,\mathrm{eV}, \tag{75}$$

while the literature values [3] read

$$\left(A_{^{87}\mathrm{Rb},^2\mathrm{S}_{1/2}}\right)_{\mathrm{lit}} = 1.413 \times 10^{-5}\,\mathrm{eV}, \tag{76}$$

$$\left(A_{^{87}\mathrm{Rb},^2\mathrm{P}_{1/2}}\right)_{\mathrm{lit}} = 1.692 \times 10^{-6}\,\mathrm{eV}, \tag{77}$$

$$\left(A_{^{85}\mathrm{Rb},^2\mathrm{S}_{1/2}}\right)_{\mathrm{lit}} = 4.185 \times 10^{-6}\,\mathrm{eV}. \tag{78}$$

For the case of ^{87}Rb, our results lie comfortably in a 1-σ environment of the literature value. The result for the $^2\mathrm{S}_{1/2}$ constant of ^{85}Rb, however, only lies inside a 4-σ environment. This is partly expected and has to do with our resolution of only six of the eight spectral lines: When considering the term schema of Rubidium (cf. fig. 1), the structure constant was calculated out of a frequency difference between the $F = 2$ to $F = (2 \text{ or } 3)$ and the $F = 3$ to $F = (2 \text{ or } 3)$ transition, mixing up the Zeeman levels of the final states. This mixing up was not accounted for in the error propagation; where the main error stems from the visual inspection of the peaks (cf. fig. 8): The error there only refers to the location of the center of the peak that one can see and does not include the fact that the peak actually consists of two peaks that are close together. Thus, while a better optical resolution of the spectral lines would increase the analysis of the hyperfine-structure constants tremendously, a more mature uncertainty on the ^{85}Rb-peaks would also help to obtain results with uncertainties that are more appropriate.

5.2. Double resonance

In this part the simultaneous radiation of the laser light and the RF transmitter to the glass cell was used to, on the one hand, determine the vertical and horizontal magnetic stray fields and, on the other hand, use this informations to determine the nuclear spins of both isotopes.

For the nuclear spin we obtained the results

$$I_{^{85}\mathrm{Rb}} = 2.51 \pm 0.03, \qquad I_{^{87}\mathrm{Rb}} = 1.49 \pm 0.03. \tag{79}$$

For ^{85}Rb the expected value is $\frac{5}{2} = 2.5$ and for ^{87}Rb it is $\frac{3}{2} = 1.5$ according to table 1, so the expectations are in a 1-σ environment of our results for both isotopes while the relative uncertainty for both results is about 2 %. So the results for this part are quiet good.

As for the magnetic stray fields we observed

$$B_{\mathrm{vert}} = (33.9 \pm 0.5)\,\mu\mathrm{T}, \qquad B_{\mathrm{hor}} = (5.6 \pm 1.1)\,\mu\mathrm{T}. \tag{80}$$

In comparison the magnetic fields of the earth given for Freiburg are [3]

$$B_{\mathrm{vert}}^{\mathrm{earth}} = 42.9\,\mu\mathrm{T}, \qquad B_{\mathrm{hor}}^{\mathrm{earth}} = 20.9\,\mu\mathrm{T}. \tag{81}$$

One can see that the magnetic stray fields measured are quite smaller than the magnetic field of the earth. One reason for this could be the influence of other stray fields overlapping with the magnetic field of the earth. Such fields could be generated by neighbouring

experiments or in general all electronics surrounding the experiment. Whether these deviations are completely explained by interfering stray fields or if the measurements done also are imprecise is hard to tell since it is not to easy to estimate all surrounding stray fields.

It is still disconcerting that the orientation of the table did not change the currents for coil 1 needed to gain equidistant absorption peaks since, if the stray field is mostly given by the magnetic field of the earth, the stray field longitudinal to the set up should have changed. However, our results are supported by the fact that the results for the nuclear spins are quite nice. So even if the currents could have been set to a value for which the peaks would have a more precise equidistant distance, the value in between the two settings of both polarities seems to be reasonable if one looks at the nuclear spin results. Additionally, while setting the currents of coil 1 it was hard to find the point of most precise equidistant distances but it was easily seen that if one setting distances as great as needed to come up with a magnetic stray field, similar to the horizontal component of the earth field given, the peaks were obviously not equidistant anymore.

5.3. Spin precession

The measurement of the spin precession turned out to be more difficult experimentally than the other parts of the experiment. However, at last we were able to get one evaluable measurement done with a compensated horizontal magnetic field from which we obtained

$$B_{\text{stray, vert}} = (32.6 \pm 1.4)\,\mu\text{T}, \tag{82}$$

which is in good agreement with the value obtained by the double resonance.

For the horizontal magnetic field we obtained two results one with a north east and one with a east orientation:

$$B_{\text{north-east}} = (4.7 \pm 0.3)\,\mu\text{T}, \qquad B_{\text{east}} = (4.9 \pm 0.4)\,\mu\text{T}. \tag{83}$$

These are not as compatible with the double resonance as the result for the vertical stray field, but are still in the same order of magnitude. The deviation of the different spin precession measurements could again be reasoned by changing stray field in the surrounding, especially since the deviations are not too big. In any case, the rough compatibility does support the significance of the results of both subtasks and the weak influence of the orientation of the experimental set up for the measurements is coherent with the observation in the double resonance that the horizontal magnetic stray field did not change much when the orientation is changed.

5.4. Relaxation time with Dehmelt's method

In order to determine the relaxation time with Dehmelt's method, the relaxation process that the ensemble undergoes after rapidly switching off the magnetic field was measured directly for various neutral filters. The neutral filters themselves were calibrated to

obtain a relative intensity I for each filter. Then, the inverse orientation time τ^{-1} obtained by an exponential fit to the relaxation process was plotted against the relative intensity and the relaxation time could be linearly extrapolated to the intercept of the linear model with the result:

$$T_{\mathrm{R}}^{^{85}\mathrm{Rb}} = (4.3 \pm 2.5)\,\mathrm{ms}, \tag{84}$$

$$T_{\mathrm{R}}^{^{87}\mathrm{Rb}} = (-5.1 \pm 2.4)\,\mathrm{ms}. \tag{85}$$

The value given in the Staatsexamen for the relaxation process of the example is 5.7 ms. While our value for $T_{\mathrm{R}}^{^{85}\mathrm{Rb}}$ lies well within a 1-σ-environment of that value, the relative error we obtained is 58 % which seems extremely high. The value we obtained for ^{87}Rb on the other hand is not only negative, but is also within a 5-σ-environment of the value from the Staatsexamen. Clearly, the values we obtained are not convincing. As the main method of obtaining the relaxation times are the linear fit depicted in fig. 13, we investigated the linear relationship more in-depth. While one can make out some linear relationship of the data by hand, there are several data points which have an extremely similar relative intensity, but differ greatly in the inverse orientation time, even when considering the error in both variables. When calculating the p-values of both intercept and slope of each fit (cf. table 8), we find that three out of the four values are above 5 %, which implies that those fit parameters are not as significant to reject the hypothesis that no linear relation exists there. This is in agreement with the visual observation that data points close in I differ greatly in τ^{-1}. Further, the residual standard error given in table 8 is suspiciously high, implying that the linear model does not fit the data very well.

Also interesting is the fact that the values that seem off the most are the values where the relative intensity I is at its maximum, $I = 1$. Unfortunately, there is a gap in relative intensities between 0.5 and 1, meaning that we can only speculate why the difference between the linear model and the data is worst at $I = 1$.

Another peculiarity we did not expect is the grave dependence of the result on the pumping light: As one can clearly see in fig. 13 and table 8, the slopes of both linear models differ drastically for the two different currents set at the laser diode. While it is reasonable to assume that the orientation time depends on the percentage of the ensemble undergoing optical pumping/relaxation (i. e. the percentage of one Rubidium isotope in the whole glass cell), we did not expect that relation to affect the slope of the linear model this drastically.

One possible explanation for the divergence from a linear relationship might lie in our calibration of the filters: As the photo diode's amplifier suddenly overloaded on the recommended DC setting on the day we calibrated the filters, the diode had to be switched to AC mode. Thus, if the measurement of the signal intensity at the oscilloscope is systematically worse for AC mode than it is for the DC mode (which is plausible in our opinion), the calibration of the filters might not be as accurate as we thought. This agrees with the observation that the absorption of some filters is extremely similar although the filters are labelled differently. A calibration of the filters in the DC mode (if even possible) – or, more general: a more thought-out calibration with a different

method altogether – would certainly be interesting.

Another difficulty that we encountered that might be correlated with the deviation from the linear relationship is the measurement of the relaxation processes. As one can see in figs. 15 and 16 in the appendix, the fits are especially askew for filters with high absorption. As one can easily see, the errors on those measurement values is especially high. Originally, we attempted to record the relaxation at a higher voltage scale, however, when inspecting the data given by the oscilloscope, we found an unanticipated "doubling"-effect: While the exponential behaviour of the relaxation was clearly visible, the measurement values also looked "doubled" and shifted upwards. An illustration of this effect is given in fig. 24. Of course, this makes it extremely impractical to fit any model onto the data which is why we chose a much smaller voltage scale. This choice, however, came with the caveat that we had to restrict our measurements to a very slim range, where the exponential behaviour was barely visible, especially for the filters with a high absorption.

What also may have contributed to the bad performance of the linear model is a wrong determination of the errors in τ^{-1} which are propagated from errors in τ which in turn were obtained from the fit to the relaxation processes already discussed in the last paragraph. While the error on each value for τ (cf. table 7) seems low, we encountered problems in obtaining the fit results as the fit's success was extremely dependent on the initial conditions, requiring a lot of trial-and-error. A more mature error estimation on the values of τ might be to take the standard deviation of the set of τ one obtains when varying the initial fit conditions for each filter separately.

All in all, we were roughly able to follow all the tasks of this part of experiment but did not manage to obtain satisfying results. While we came up with some possible explanations, we did not manage to single out an exact underlying problem.

5.5. Relaxation time with Franzen's method

An alternative method to determine the relaxation time is given by Franzen's method: Here, the relaxation process was not initiated by a change in the magnetic field but rather by interrupting the pumping light to the system.

After determining the relative intensity of the system for varying dark times, we were able to fit an exponential model to the intensity with respect to the dark times. Our fit directly supplied us with the relaxation time of

$$T_{\mathrm{R}} = (8.5 \pm 2.5)\,\mathrm{ms}. \tag{86}$$

Compared to the value given in the Staatsexamen of 5.7 ms, our value lies comfortably in a 2-σ-environment, but the relative error of our result (34 %) is quite high. While our obtained result is definitely compatible with the literature value, we want to comment on some of the techniques of Franzen's method.

For one, it is extremely hard to determine the exact time the system starts pumping again (these times are marked with a red cross in figs. 17 and 18) as the signal of the photo diode does not increase sharply at all, but is rather unhasting. In the oscilloscope signal this can be seen as a linear process turning into an exponential saturation which is not

easy to pin-point. That the method is not highly reliable can also be seen in the outlier in fig. 14 at about $\Delta t = 3.76\,\text{ms}$ which can be reasonably explained by a misjudgment on our part when determining the point where pumping occurs again (compare with the plot on the bottom right in fig. 17). Outliers like these may also explain the high error of the fit and with that the high uncertainty of our result. Also, note that for dark times shorter than $\Delta t = 2\,\text{ms}$ we were not able to determine the point at which the signal turns into exponential saturation at all.

Enhancing the reliability of this method may go well with the use of a less inert photo diode or in focussing the laser beam better on the Rubidium cell such that the transition time of the chopper from shut to open is reduced.

To summarize, we were able to carry out this part of the experiment and obtain a value that, although compatible with the literature, has a high uncertainty. Our main issue we encountered when using this method is the reliance on determining the location of the intensity after the dark time which comes close to effectively guessing for some spectra.

As our determination of the relaxation time using Dehmelt's method seems inconsistent in itself – having obtained clearly conflicting results in eqs. (84) and (85) with one of them physically impossible –, it is difficult to compare it to Franzen's method. As our relative errors for all results regarding the relaxation times lie above 30 %, it is intricate to attribute a high significance to our result. Nevertheless, we want to briefly compare the fundamental systematic differences between both methods. Dehmelt's method relies on extrapolating the orientation time of orientation process for different pumping light intensities. Therefore, it is critical to obtain measurements for each pumping light intensity where the orientation time can be extracted cleanly (which we were not able to do especially for low-intensity filters as described in section 5.4). Further, a knowledge of the filter's absorption is necessary, which we attained by further measurements (cf. section 4.4.1).

While Franzen's method, on the other hand, also relies on taking measurements where the intensity and dark time can be extracted as cleanly as possible, the extraction was done visually in our case (in contrast to, say, curve fits) which brings even more inconsistencies in the analysis with itself. This can be clearly seen by the outliers in fig. 14, for example. Experimentally, Dehmelt's method seems to be more robust: Switching off the magnetic field happens quite quickly and abrupt as one can see in the measurements displayed in figs. 15 and 16. The chopper used for Franzen's method, on the other hand, doesn't show the same abruptness as one can see in figs. 17 and 18, with the intensity behaviour even showing a non-linear behaviour which makes it even more difficult to extrapolate the points critical for the analysis.

List of Figures

List of Tables

References

[1] Clemens Baur. *Einrichtung des Versuches "Optisches Pumpen mit Laserdioden"*. Fakultät für Physik, Albert-Ludwigs-Universität Freiburg, 1997.

[2] Jones; Eric, Travis Oliphant, Pearu Peterson, et al. *SciPy: Open source scientific tools for Python*. Online; Accessed on Aril 2nd, 2021. 2001–. URL: https://www.scipy.org/.

[3] M. Köhli. *Optisches Pumpen. Fortgeschrittenen Praktikum II*. 2012.

[4] R Core Team. *R: A Language and Environment for Statistical Computing*. R Foundation for Statistical Computing. Vienna, Austria, 2021.

[5] S. A. *Digital Oscilloscope Series DS1000Z*. Online; Accessed on Aril 14nd, 2021. 2020-05. URL: https://www.rigol-uk.co.uk/jg/wp-content/uploads/2020/09/Rigol-DS1000Z-Datasheet.pdf.

A. Appendix

Table 10: Absolute and relative intensities of each filter used for determining the relaxation time using Dehmelt's method.

Filter	U^{Abs} [V]	I
None	0.251 ± 0.004	1
d0_3	0.1272± 0.0022	0.506± 0.011
d0_6	0.1084± 0.0012	0.431± 0.008
d1_0	0.0528± 0.0019	0.210± 0.008
d1_3	0.0338± 0.0010	0.134± 0.004
d1_6	0.0400± 0.0013	0.159± 0.006
d2_0	0.0258± 0.0014	0.103± 0.006
d2_6	0.0216± 0.0013	0.086± 0.005
d-0_37	0.0816± 0.0014	0.501± 0.011
d-0_8	0.0350± 0.0015	0.214± 0.009

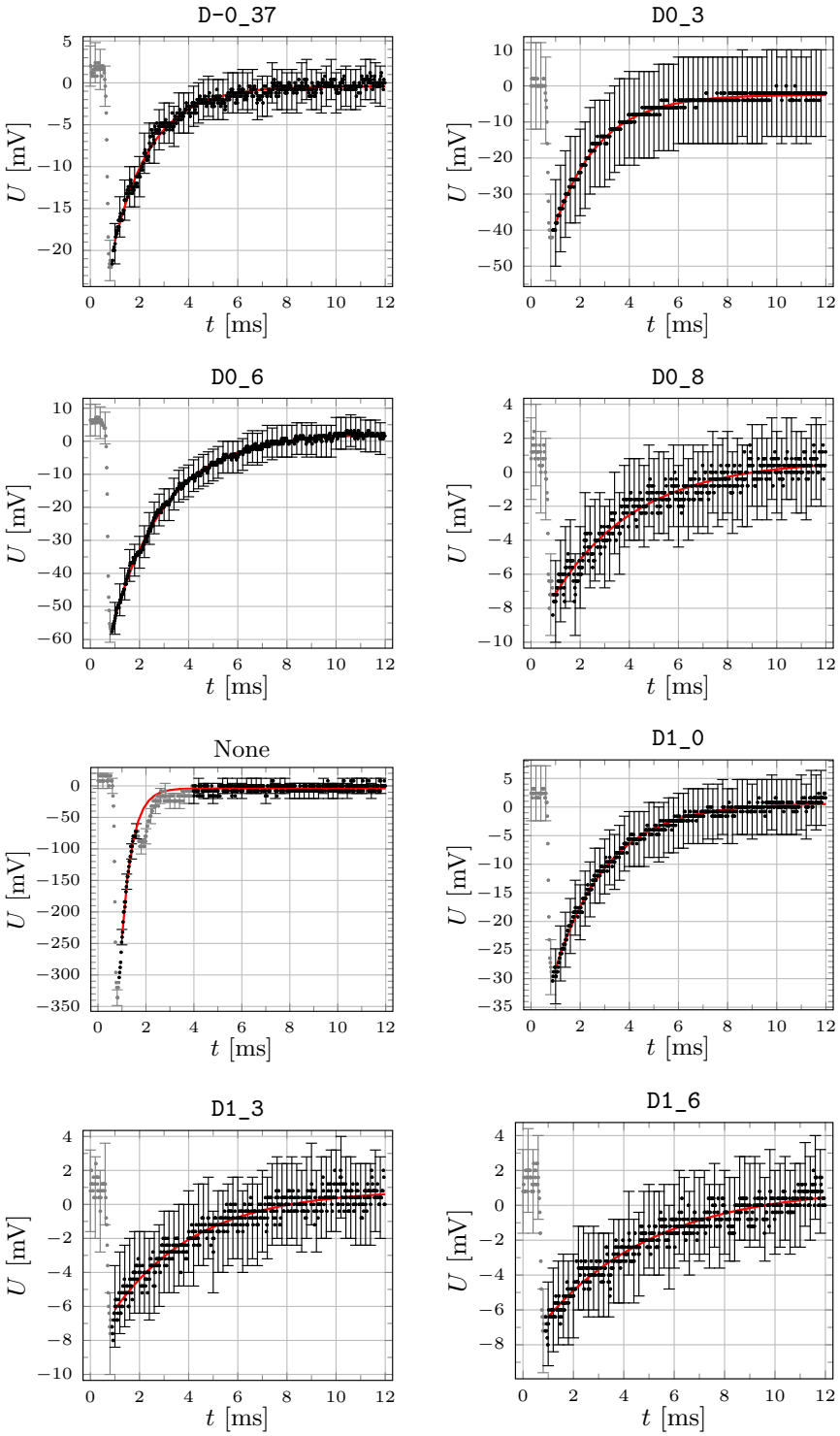

Figure 15: Exponential saturation fits on various filters for the ^{85}Rb isotope.

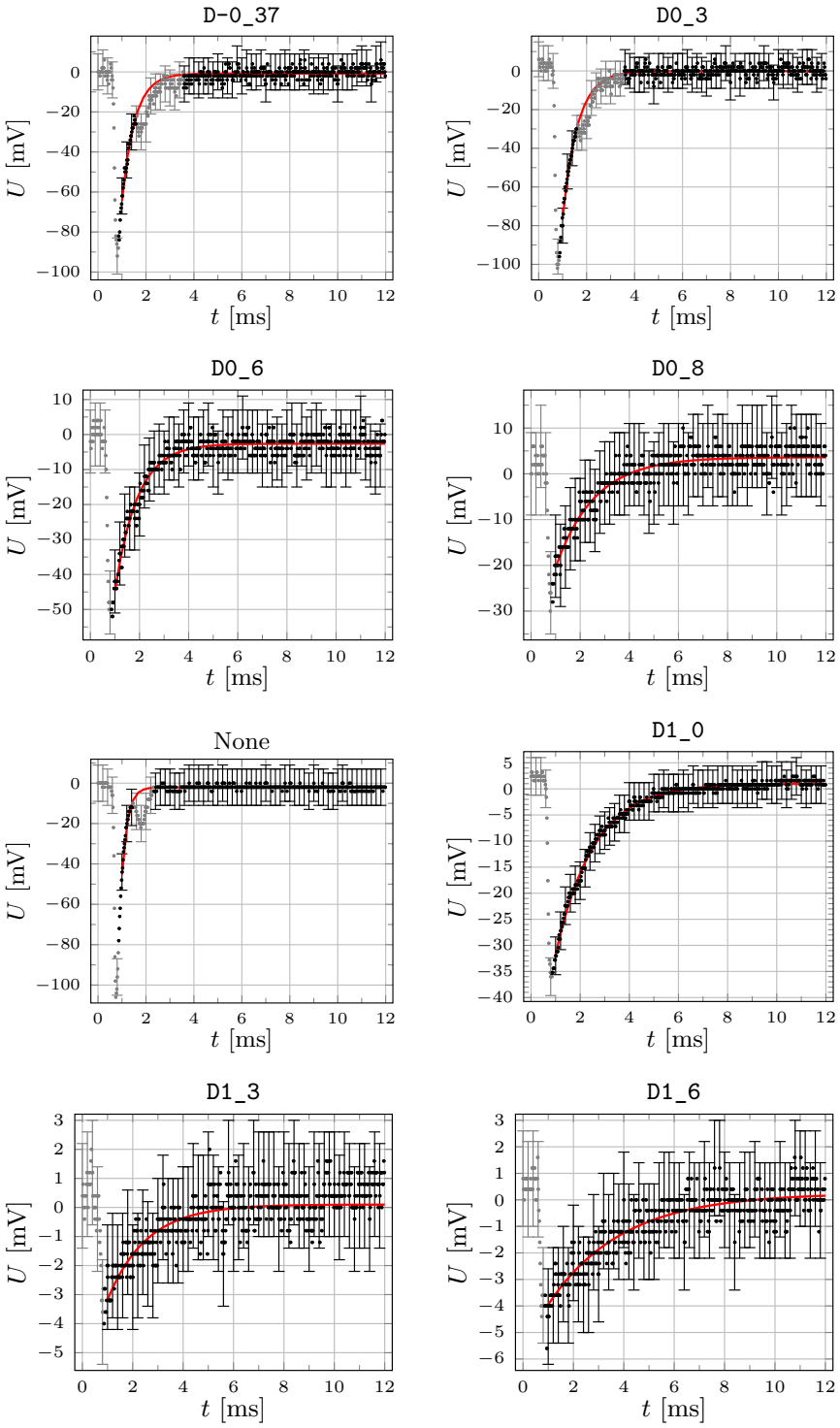

Figure 16: Exponential saturation fits on various filters for the ^{87}Rb isotope.

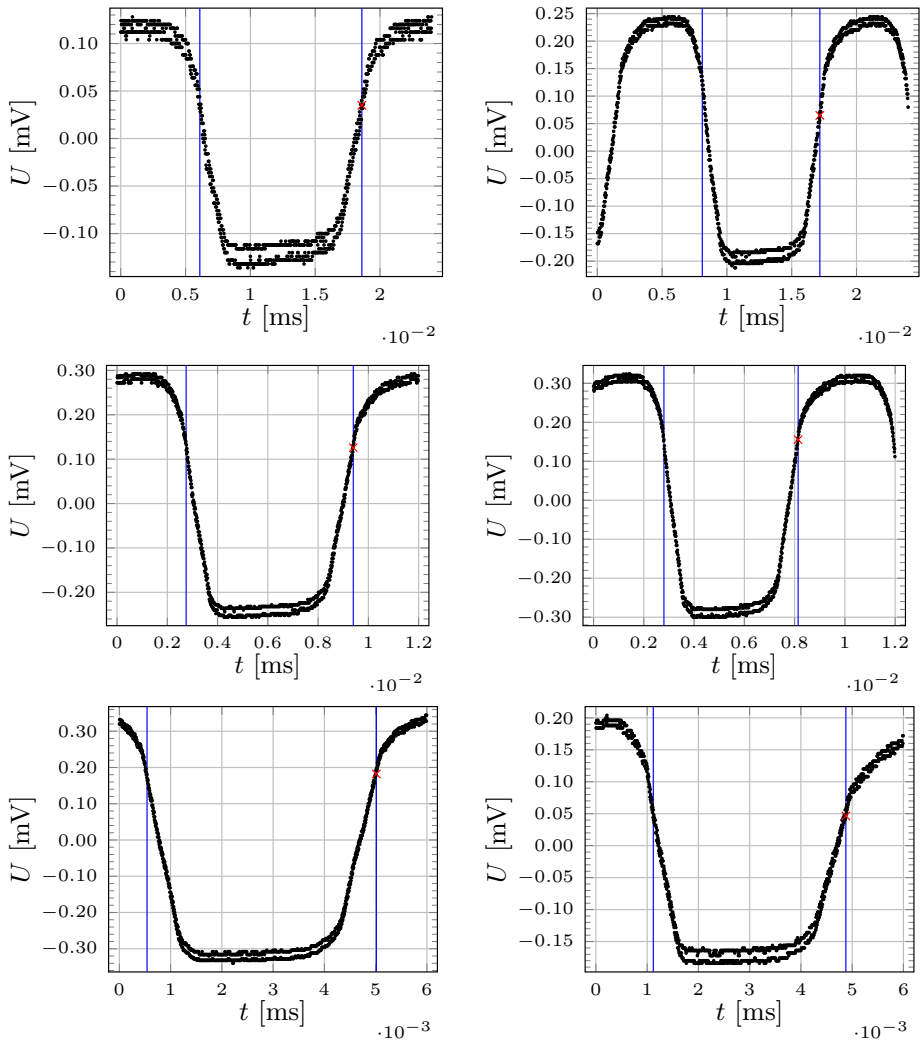

Figure 17: Visual examination of the dark time Δt and the corresponding intensity $U^{\text{abs}}(\Delta t)$ for various chopper speeds.

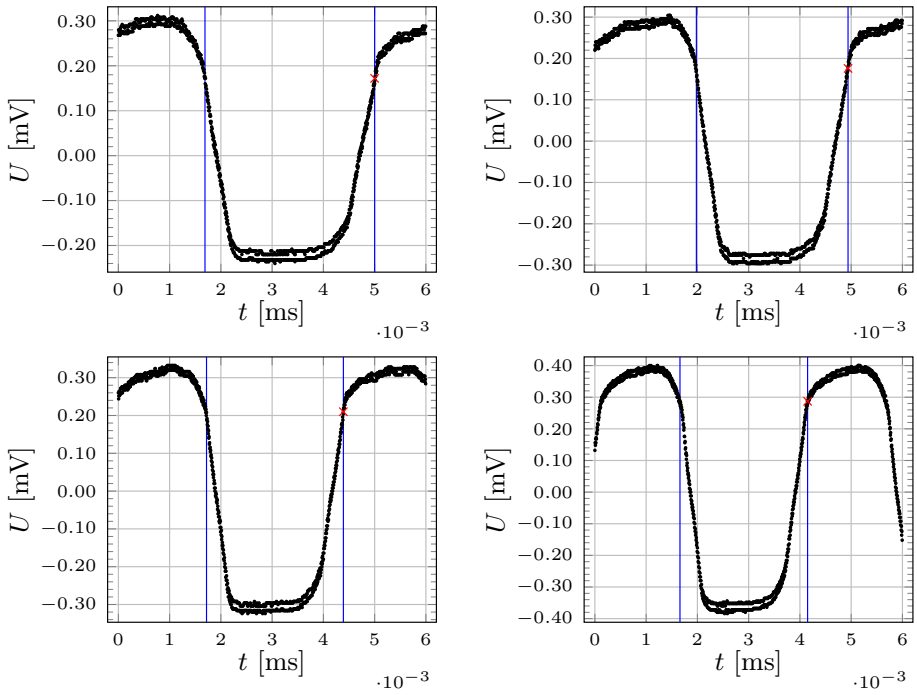

Figure 18: Visual examination of the dark time Δt and the corresponding intensity $U^{\text{abs}}(\Delta t)$ for various chopper speeds (cont. of fig. 17).

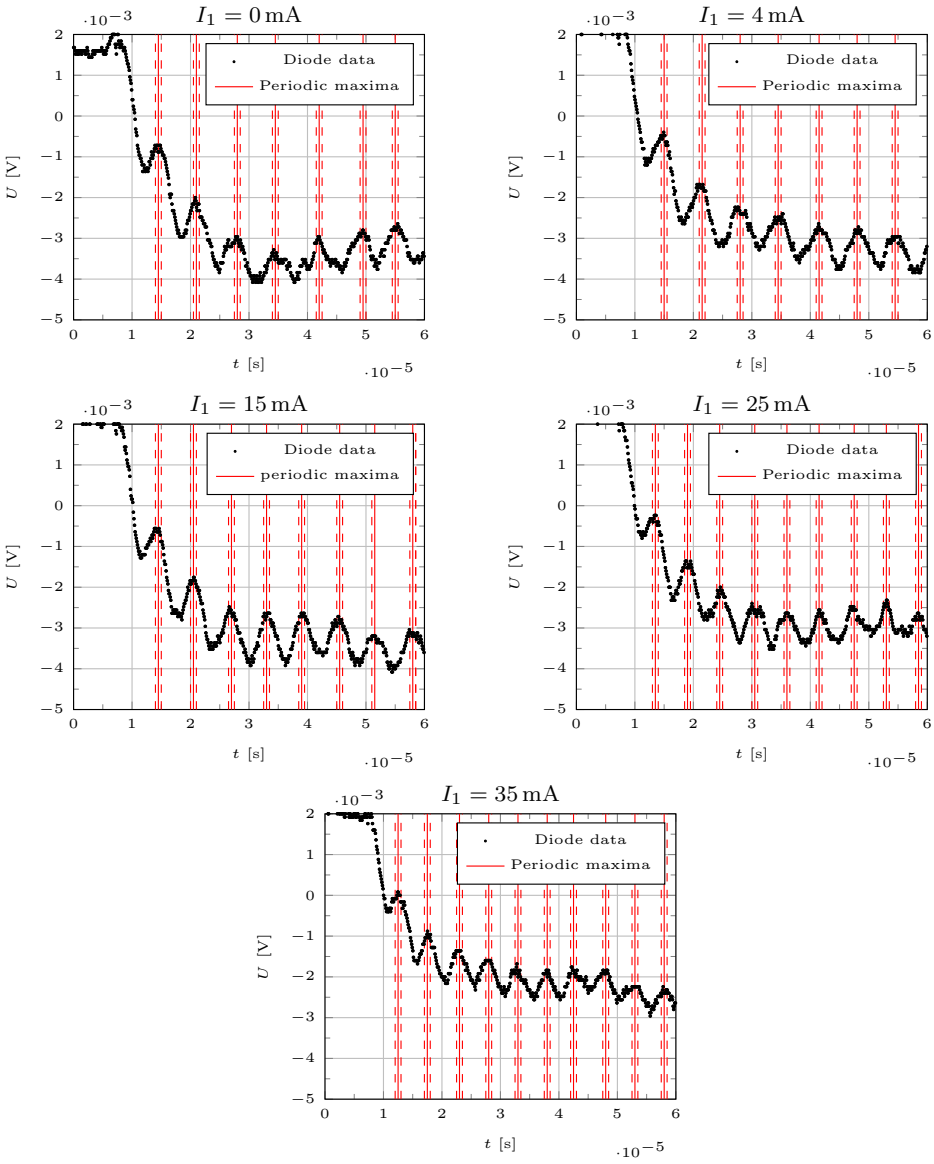

Figure 19: In this plots the measurements of the spin precession are shown with the current in coil four set to zero while the longitudinal axis of the experimental set up is directed to the north east. The current in coil one differs from plot to plot with upper left 0 mA, upper right 4 mA, middle left 15 A, middle right 25 mA and bottom 35 mA.

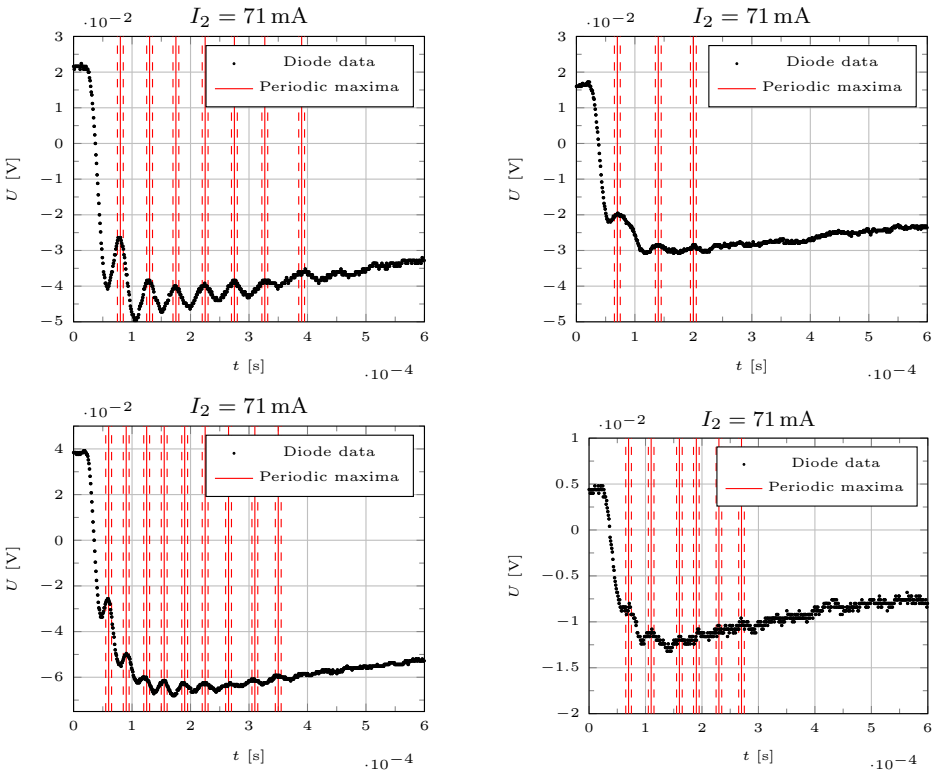

Figure 20: In this plots the measurements of the spin precession are shown with the current in coil one set to zero while the longitudinal axis of the experimental set up is directed to the northeast and the current of coil 4 is set to 71 mA.

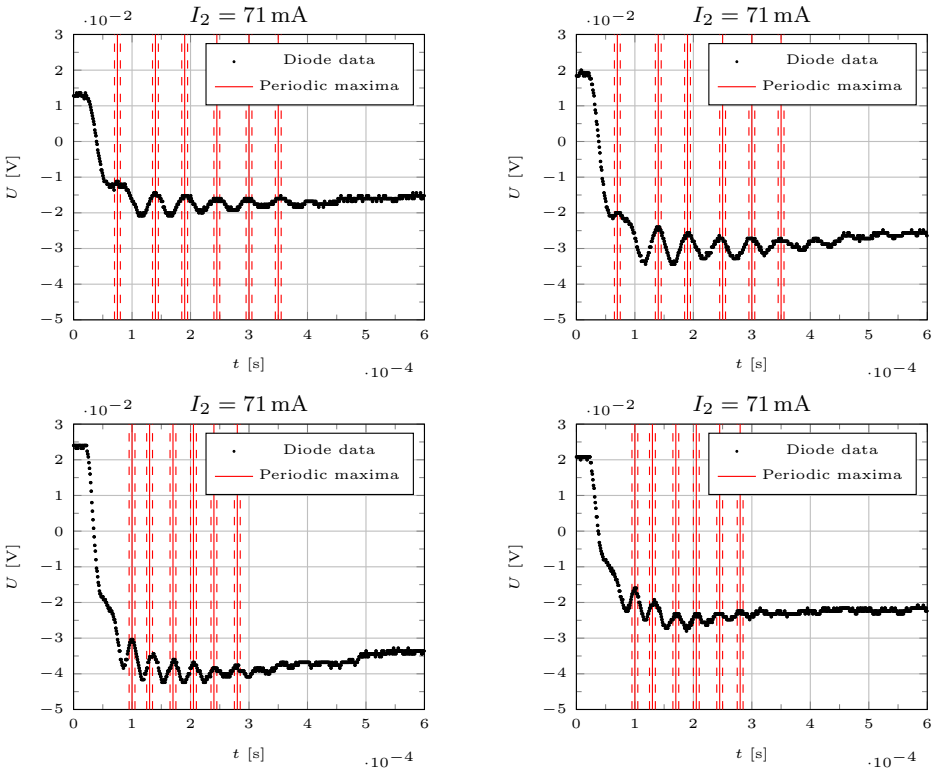

Figure 21: In this plots the measurements of the spin precession are shown with the current in coil one set to zero while the longitudinal axis of the experimental set up is directed to the east and the current of coil 4 is set to 71 mA.

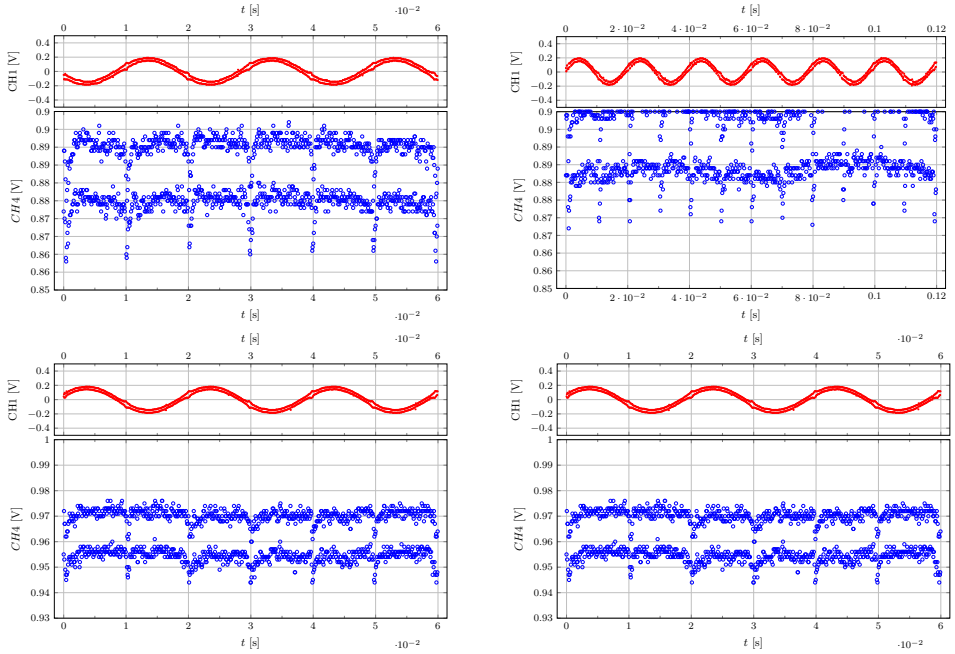

Figure 22: The setting for the equidistant peaks in the double resonance task. For each plot the upper red plot shows the sinusoidal signal of coil 2, while the lower blue plots show the signal of the PD. The two upper plots are with the laser setting for ^{85}Rb, on the left side with $I_1 = 132\,\text{mA}$ and on the right side with $I_1 = 139\,\text{mA}$. The two bottom plots are with the laser settings for ^{87}Rb, on the left side with $I_1 = 86\,\text{mA}$ and on the right side with $I_1 = 93\,\text{mA}$.

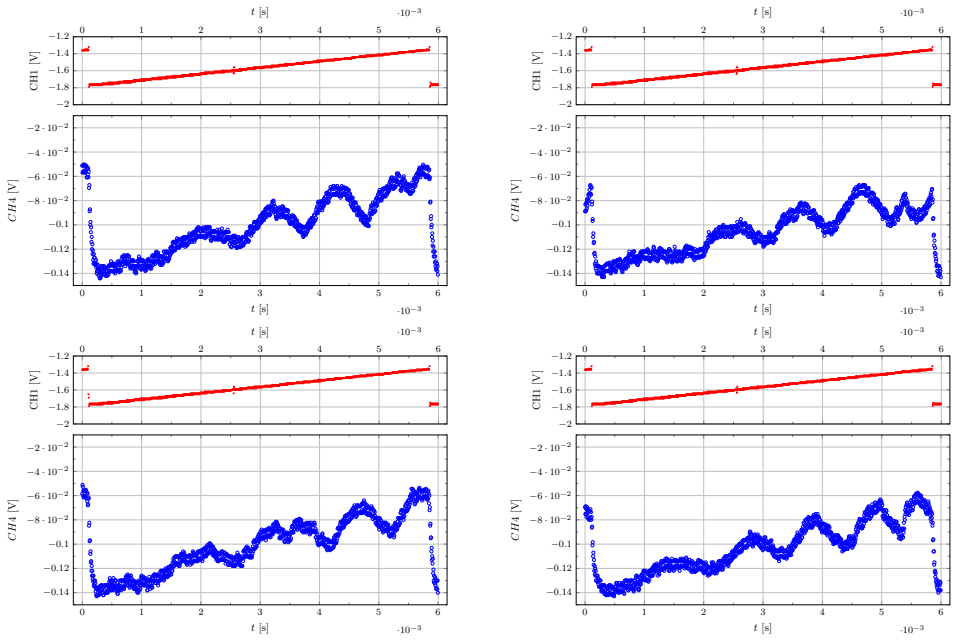

Figure 23: The PD signal with the etalon mounted to the bench for different temperatures. Upper left $T = 34.6\,^{\circ}\mathrm{C}$, upper right $T = 34.8\,^{\circ}\mathrm{C}$, bottom left $T = 36.0\,^{\circ}\mathrm{C}$ and bottom right $T = 36.9\,^{\circ}\mathrm{C}$. For each plot the ramp signal of the laser is shown in red above.

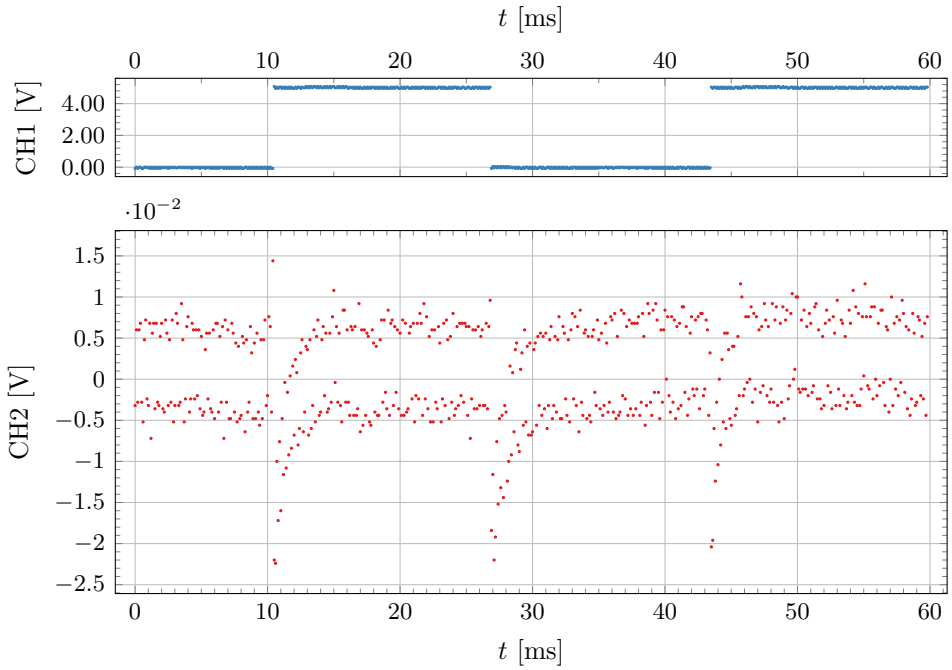

Figure 24: Unanticipated effect in the oscilloscope data of the relaxation process with a large voltage range (unused for the analysis).

B. Lab Notes

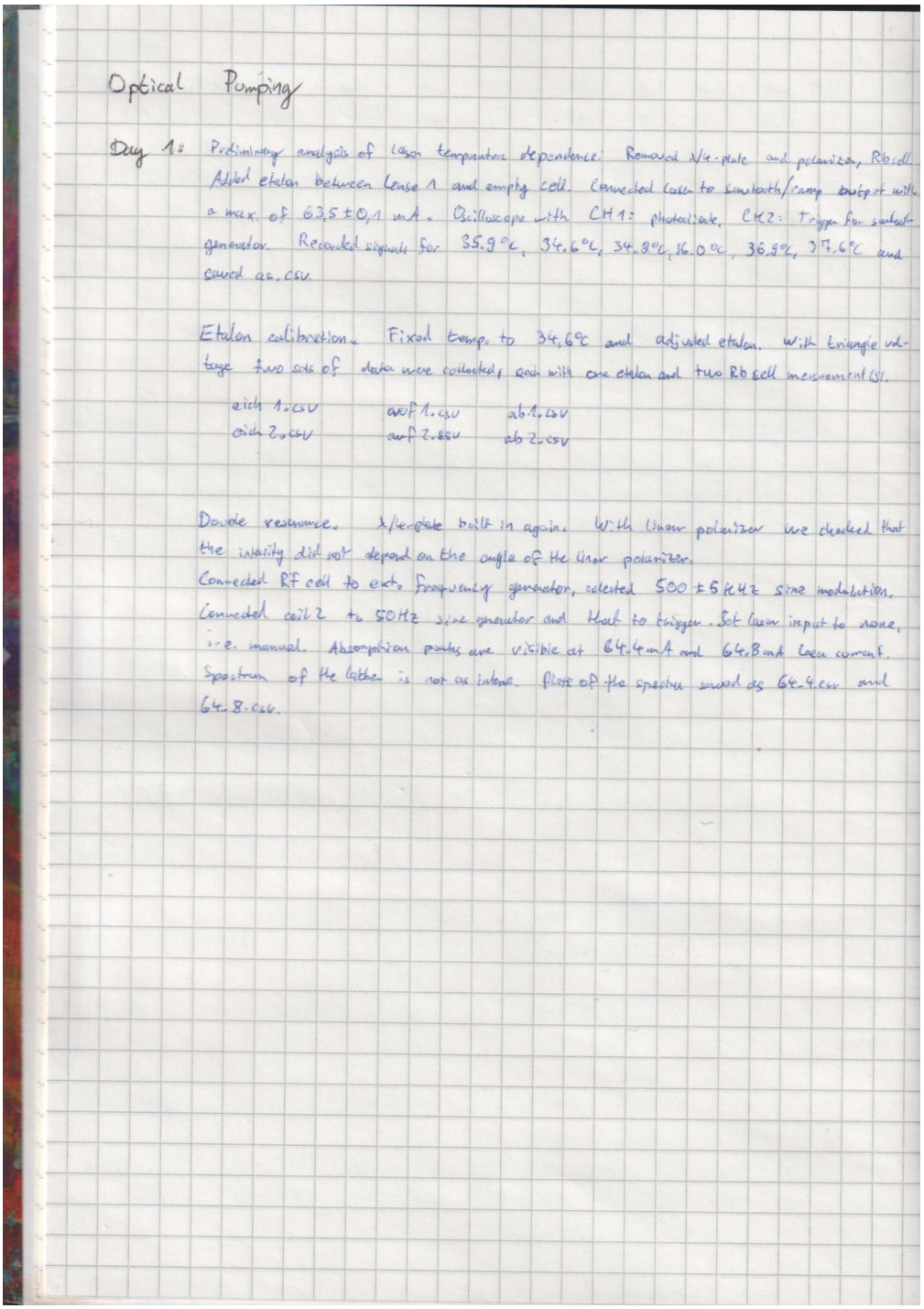

Optical Pumping

Day 1: Preliminary analysis of laser temperature dependence. Removed λ/4-plate and polarizer, Rb cell. Added etalon between Lense 1 and empty cell. Connected laser to sawtooth/ramp output with a max. of 63,5 ± 0,1 mA. Oscilloscope with CH1: photodiode, CH2: Trigger for sawtooth generator. Recorded signals for 35.9°C, 34.6°C, 34.8°C, 36.0°C, 36.9°C, 37.6°C and saved as .csv.

Etalon calibration. Fixed temp. to 34,6°C and adjusted etalon. With triangle voltage two sets of data were collected, each with one etalon and two Rb cell measurements.

eich 1.csv	auf 1.csv	ab 1.csv
eich 2.csv	auf 2.csv	ab 2.csv

Double resonance. λ/4-plate built in again. With linear polarizer we checked that the intensity did not depend on the angle of the linear polarizer.
Connected RF coil to ext. frequency generator, selected 500 ± 5 kHz sine modulation. Connected coil 2 to 50Hz sine generator and Hook to trigger. Set laser input to none, i.e. manual. Absorption peaks are visible at 64.4 mA and 64.8 mA laser current. Spectrum of the latter is not as intense. Plots of the spectra saved as 64.4.csv and 64.8.csv.

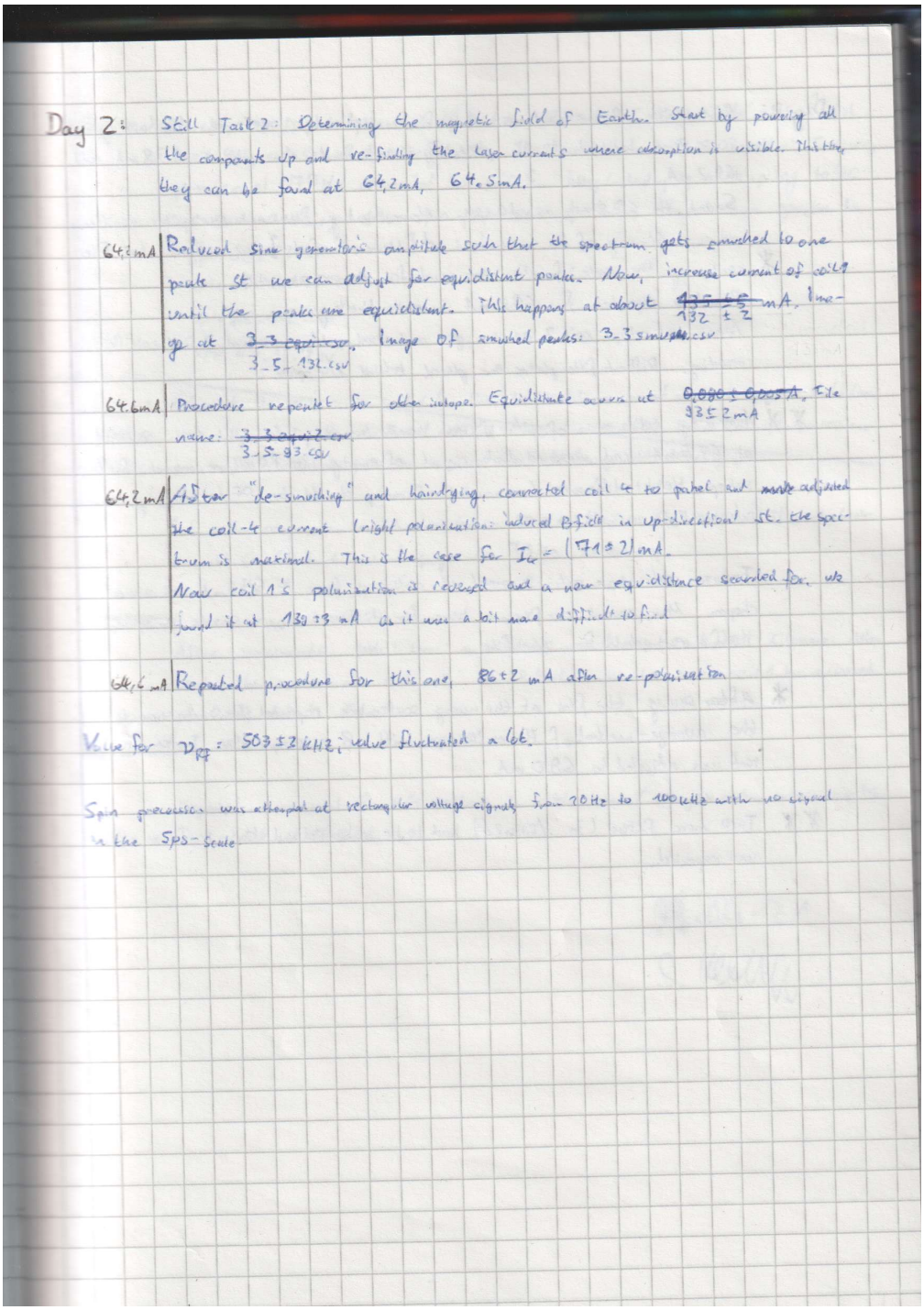

Day 2: Still Task 2: Determining the magnetic field of Earth. Start by powering all the components up and re-finding the laser currents where absorption is visible. This time, they can be found at 64,2 mA, 64,5 mA.

64,2 mA | Reduced sine generator amplitude such that the spectrum gets smushed to one peak st we can adjust for equidistant peaks. Now, increase current of coil 4 until the peaks are equidistant. This happens at about ~~[illegible]~~ 132 ± 2 mA. Image up at ~~3_3 [illegible]~~ 3_5_132.csv. Image of smushed peaks: 3_3 smushed.csv

64,6 mA | Procedure repeated for other isotope. Equidistance occurs at ~~0,090 ± 0,005 A~~ 93 ± 2 mA. File name: ~~3_3 equi2.csv~~ 3_5_93.csv

64,2 mA | After "de-smushing" and hairdrying, connected coil 4 to pabel and ~~made~~ adjusted the coil-4 current (right polarization: induced B-field in up-direction) st. the spectrum is maximal. This is the case for I_{c4} = (171 ± 2) mA.
Now coil 1's polarization is reversed and a new equidistance searched for. We found it at 139 ± 3 mA as it was a bit more difficult to find.

64,6 mA | Repeated procedure for this one. 86 ± 2 mA after re-polarization

Value for ν_{eff}: 503 ± 2 kHz; value fluctuated a lot.

Spin precession was observed at rectangular voltage signals from 20 Hz to 100 kHz with no signal in the 5ps-scale.

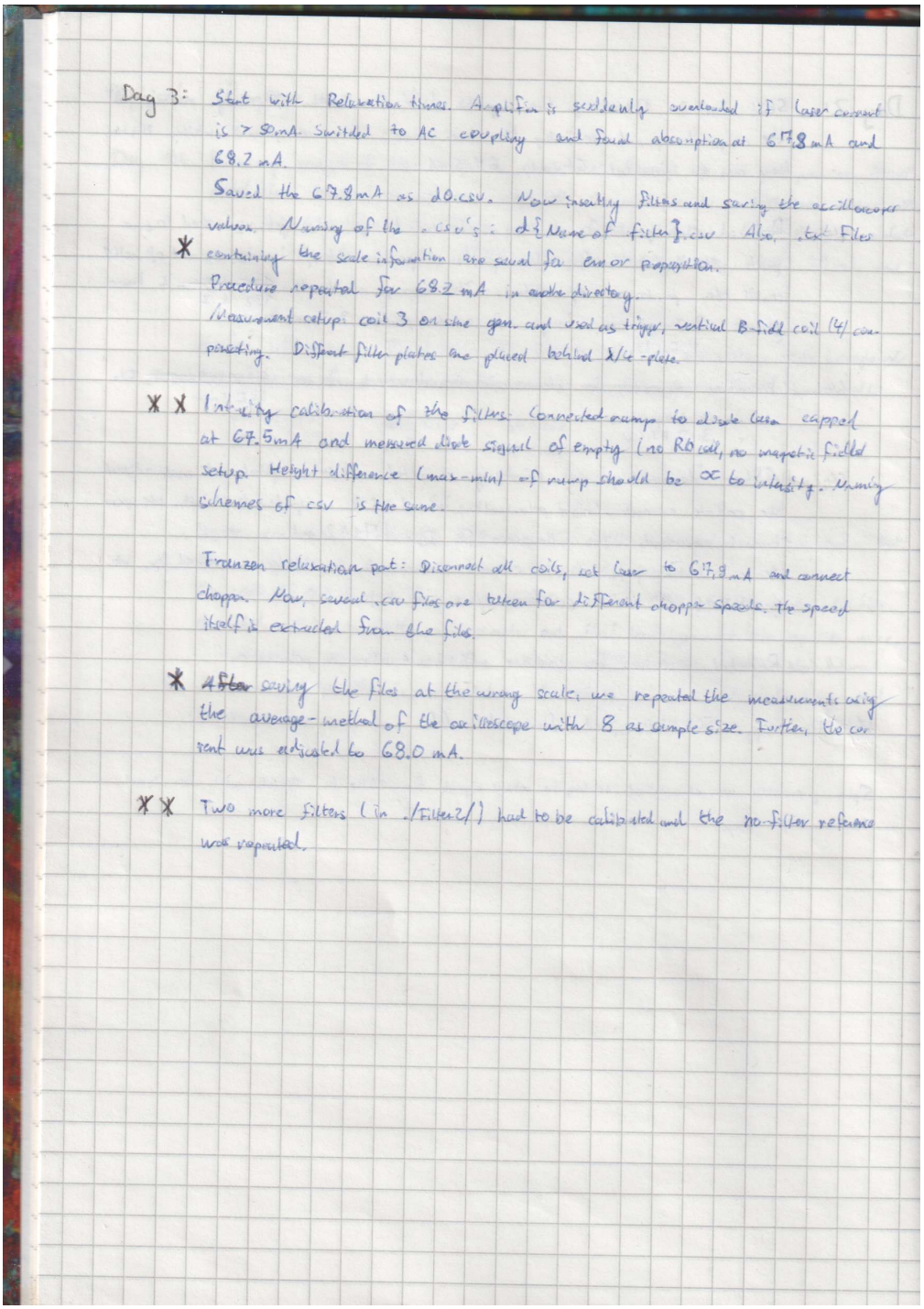

Day 3: Start with Relaxation times. Amplifier is suddenly overloaded if laser current is > 90mA. Switched to AC coupling and found absorption at 67.8 mA and 68.2 mA.

Saved the 67.8 mA as d0.csv. Now inserting filters and saving the oscilloscope values. Naming of the .csv's: d[Name of filter].csv Also, .txt files containing the scale information are saved for error propagation.

* Procedure repeated for 68.2 mA in another directory.

Measurement setup: coil 3 on sine gen. and used as trigger, vertical B-field coil (4) connecting. Different filter plates are placed behind λ/4-plate.

** Intensity calibration of the filters: Connected pump to diode laser capped at 67.5mA and measured diode signal of empty (no Rb cell, no magnetic field) setup. Height difference (max-min) of pump should be ∝ to intensity. Naming schemes of csv is the same.

Franzen relaxation part: Disconnect all coils, set laser to 67.9 mA and connect chopper. Now, several .csv files are taken for different chopper speeds. The speed itself is extracted from the files.

* ~~After~~ saving the files at the wrong scale, we repeated the measurements using the average-method of the oscilloscope with 8 as sample size. Further, the current was adjusted to 68.0 mA.

** Two more filters (in ./Filter2/) had to be calibrated and the no-filter reference was repeated.

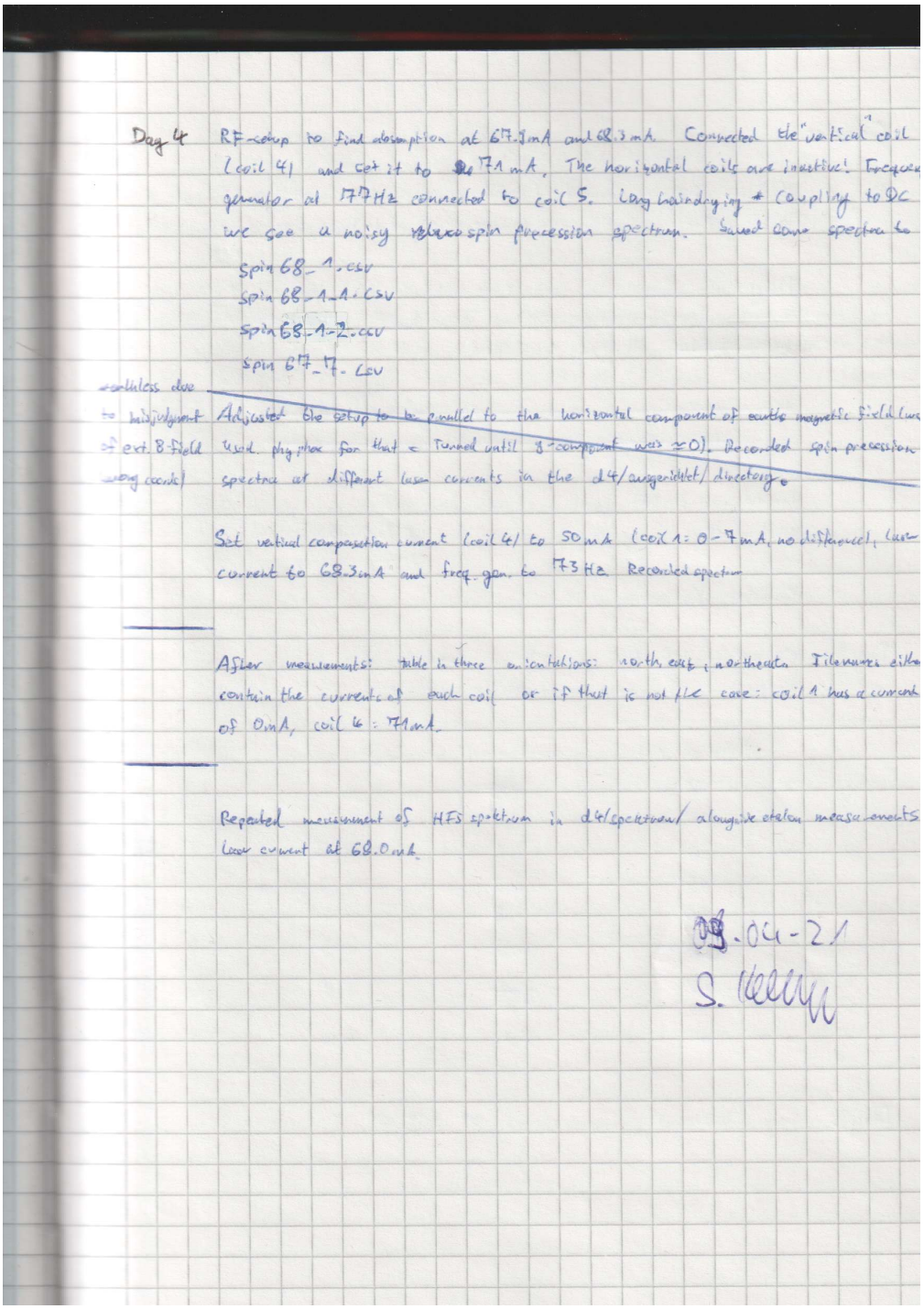

Day 4 RF-setup to find absorption at 67.3 mA and 68.3 mA. Connected the "vertical" coil (coil 4) and set it to 71 mA. The horizontal coils are inactive. Frequency generator at 177 Hz connected to coil 5. Long twisted wire coupling to DC we see a noisy ~~electro~~ spin precession spectrum. Saved some spectra to

spin 68_1.csv
spin 68_1_A.csv
spin 68_1_2.csv
spin 67_1.csv

~~endless due to misjudgment of ext. B-field using coils~~ Adjusted the setup to be parallel to the horizontal component of earths magnetic field (was used physics for that = Turned until B-component was ≈0). Recorded spin precession spectra at different laser currents in the d4/ausgerichtet/ directory.

Set vertical compensation current (coil 4) to 50 mA (coil 1: 0.7 mA, no difference), laser current to 68.3 mA and freq. gen. to 173 Hz. Recorded spectrum

---

After measurements: table in three combinations: no-th, exp, no-theo. Filenames either contain the currents of each coil or if that is not the case: coil 1 has a current of 0 mA, coil 4: 71 mA.

Repeated measurement of HFS spektrum in d4/spektrum/ alongside etalon measurements. Laser current at 68.0 mA.

09.04-21
S. [illegible]